10th International Workshop on Microsystems

Alexander Campus, International Hellenic University, 08 December 2025

Workshop Proceedings

Introduction

This workshop brings together research and development from a large spectrum of science and engineering fields related to the implementation of microsystems in the new era of distributed information technologies. As cloud computing services and smart portable systems are becoming ubiquitous and more advanced, new possibilities for interdisciplinary research emerge. The microsystems that comprise the so-called internet of things will encompass a wide range of technologies including new energy sources, energy and information electronics, sensor systems, smart and energy efficient control and computing, telecommunications and networking, and also nanotechnology and micro-electro-mechanical systems. Continuing nine successful workshops between 2016 and 2024, the 10th International Workshop on Microsystems aims at bringing together related research and development advancements from the academic community and the industry. Scientific topics include but are not limited to:

Microelectronics and nanoelectronics	Industrial automation and control
Embedded systems	Micro-electro-mechanical systems
Sensors and sensor electronics	Computing for microsystems
Integrated circuits and systems	Energy microsystems

Michail E. Kiziroglou
m.kiziroglou@ihu.gr

Venue

Lecture Theater, Automation and Informatics Building
Alexander Campus, International Hellenic University, Greece

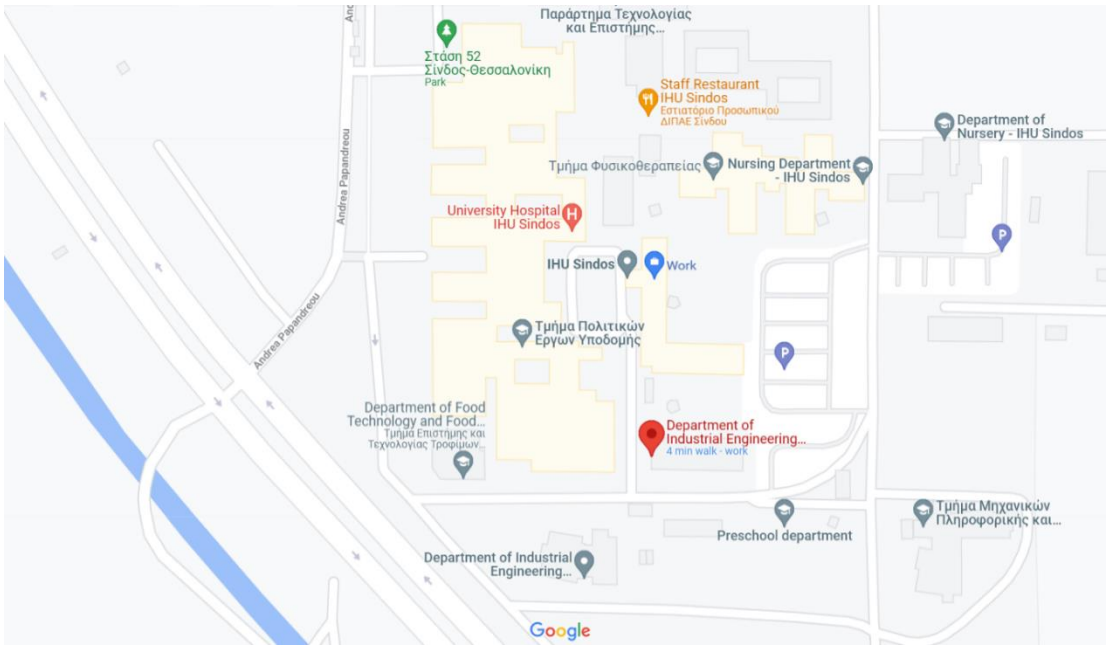

Date

Monday, 8th of December, 2025

Organizer

Michail E. Kiziroglou

Session Chairs

Dr. Nikolaos Tampouratzis, Industrial Engineering & Management, IHU, Greece
Dr. Dimitrios Triantafyllidis, Industrial Engineering & Management, IHU, Greece
Dr. Maria S. Papadopoulou, Information and Electronic Engineering, IHU, Greece
Dr. Theodoros Kosmanis, Industrial Engineering & Management, IHU, Greece
Dr. Dimitrios Tziourtzioumis, Industrial Engineering & Management, IHU, Greece

Technical Programme Committee

Alexandros Astaras
Dimitrios Bechtsis
Alkiviadis Hatzopoulos
Michail E. Kiziroglou
Theodoros Kosmanis
Simira Papadopoulou
Kostas Siozios
Fotis Stergiopoulos
Nikolaos Tampouratzis
Dimitrios Tziourtzioumis
Apostolos Tsagaris
Dimitrios Triantafyllidis
Christos Yfoulis

Local Organizing Committee

M. E. Kizirogou, E. Aivazidou, I. Kochliaridis, M. Michaelidou and E. Kapetangiorgi

List of Authors

No	Last Name	First Name	Affiliation
1	Alonso	Jaime G.	Airbus Defence and Space, Spain
2	Anagnostaki	Filliana	IEM, International Hellenic University, Greece
3	Athanasiadis	Angelos	Aristotle University of Thessaloniki, Greece
4	Aubakirova	Aliyara	University of Messina, Italy
5	Berguerand	Robin	CSEM, Switzerland
6	Candelotto	Adrien	Serma Ingenierie, France
7	Carriere	Alexis	Serma Ingenierie, France
8	Dallemagne	Philippe	CSEM, Switzerland
9	Doulaki	Paraskevi	IEM, International Hellenic University, Greece
10	Hatzopoulos	Argyrios T.	IEE, International Hellenic University, Greece
11	Holmes	Andrew S.	Imperial College London, U.K.
12	Iniesta	Daniel	Airbus Defence and Space, Spain
13	Kiziroglou	Michail E.	IEM, International Hellenic University, Greece
14	Kochliaridis	Ippokratis	IEM, International Hellenic University, Greece
15	Kosmanis	Theodoros I.	IEM, International Hellenic University, Greece
16	Marty	David	Serma Ingenierie, France
17	Minas	D.	IEE, International Hellenic University, Greece
18	Mitsitsikas	Dimitrios	Olympia Electronics, Greece
19	Mousouliotis	Panagiotis	Aristotle University of Thessaloniki, Greece
20	Ouzounis	Dimitrios	IEE, International Hellenic University, Greece
21	Papadopoulou	Maria S.	IEE, International Hellenic University, Greece
22	Papaefstathiou	Ioannis	Aristotle University of Thessaloniki, Greece
23	Piguet	Damien	CSEM, Switzerland
24	Siakas	I.	IEM, International Hellenic University, Greece
25	Soudris	Dimitrios	National Technical University of Athens, Greece
26	Tampouratzis	Nikolaos	IEM, International Hellenic University, Greece
27	Triantafyllidis	Dimitris	IEM, International Hellenic University, Greece
28	Tsiakmakis	Kyriakos	IEE, International Hellenic University, Greece
29	Tsintotas	Konstantinos	IEE, International Hellenic University, Greece
30	Tziourtzioumis	Dimitrios N.	IEM, International Hellenic University, Greece
31	Vassios	V. D.	IEE, International Hellenic University, Greece
32	Wright	Steven W.	Imperial College London, U.K.
33	Xenofontos	George	IEM, International Hellenic University, Greece
34	Yeatman	Eric M.	University of Glasgow, U.K.

Programme

08:45-09:15: Registration

Please check-in or register at the front desk.

09:15-09:30: Welcome and introduction

09:30-10:40: First Oral Session (Session Chair: Nikolaos Tampouratzis, IHU)

09:30-10:10: FPGA Acceleration for Vision-Based Navigation in Space Applications: Algorithms & Use Cases, *D. Soudris, National Technical University of Athens,Greece* 25WOM-01 (Invited)

10:10-10:25: FUSION: A Full-System Network Co-Simulation Framework, *A. Athanasiadis, N. Tampouratzis, I. Papaefstathiou*, 25WOM-02

10:25-10:40: Automated Hydroponic Greenhouse for Fodder Production, *I. Siakas and D. Triantafyllidis,* 25WOM-03

10:40-11:10: Coffee Break and Poster Session (Session Chair: D. Triantafyllidis)

P1. Electronically Controlled Distillation Chamber with Integrated IoT System, *D. Ouzounis, K. Tsiakmakis, M. S. Papadopoulou, V.D. Vassios, K.A. Tsintotas and A.T. Hatzopoulos*, 25WOM-04

P2. Measuring the resonance frequency and attenuation of Polyvinylidene Fluoride (PVDF) beams, *I. Kochliaridis and M. E. Kiziroglou*, 25WOM-05

P3. A Camera-based Portable Scattering Analyser Towards Blood Cell Photoplethysmography, *E. Kapetangiorgi and M. E. Kiziroglou,* 25WOM-06

P4. Aircraft Structural Health Multi-Sensor Wireless Node Powered by Energy Harvesting, *J. G. Alonso, R. Berguerand, A. Candelotto, A. Carriere, Ph. Dallemagne, A. S. Holmes, D. Iniesta, M. E. Kiziroglou, D. Marty, D. Piguet, S. W. Wright and E. M. Yeatman*, 25WOM-07

11:10-12:35: Second Oral Session (Session Chair: M. S. Papadopoulou, IHU)

11:10-11:50: Building a Safer Future with Olympia Electronics, *S. Theodorou and D. Mitsitsikas*, 25WOM-08 (Invited)

11:50-12:05: Analysis of Operational Deviations and Their Implications for the Steady-State Assumption in Small-Scale R134a Refrigeration Cycles, *A. Aubakirova and D. Tziourtzioumis*, 25WOM-09

12:05:-12:20: An Online Framework for Quality Control, Anomaly Detection and Auto-Calibration of Hourly Air-Quality Data from an IoT Sensor Node, D. *Minas, K. Tsiakmakis, A. T. Hatzopoulos, M. S. Papadopoulou and V. Vassios,* 25WOM-10

12:20-12:35: Seismic Activity Detection with ESP32 Microcontroller using TinyML*, G. Xenofontos, K. Tsiakmakis, A. T. Hatzopoulos and M. S. Papadopoulou*, 25WOM-11

…Continued overleaf !

12:35 – 13:30 Third Oral Session (Session Chairs: Th. Kosmanis and D. Tziourtzioumis, IHU)

12:35-12:55: Parameterizable FPGA Accelerator Design for Embedded Deep Learning, *Panagiotis Mousouliotis, Aristotle University of Thessaloniki*, 25WOM-12 (Invited)

12:55-13:10 Erasmus+ MSc Course: Intelligent Sustainable Habitats, *F. Anagnostaki, Th. Kosmanis and D. Tziourtzioumis*, 25WOM-13

13:10-13:25 HORIZON-MSCA project: Integration of Advanced Experiments, Computation and Data for Innovation in Freeze Casting and Advanced Porous Structures, *Th. Kosmanis and D. Tziourtzioumis*, 25WOM-14

13:25-13:40 Erasmus+ MSc Course: Smart Sustainability Solutions, *D. Tziourtzioumis and Th. Kosmanis,* 25WOM-15

13:40-13:50: Best Paper Award by Ioannidis Electronics.

WORKSHOP PAPERS

Speaker:

FPGAAcceleration For Vision-Based Navigation in Space Applications: Algorithms & Use Cases

Prof. Dimitrios Soudris
School of Electrical and Computer Eng.
National Technical Univ. of Athens, Greece
dsoudris@microlab.ntua.gr

Abstract: The webinar exploits will present the advent of field-programmable gate arrays (FPGAs) to accelerate the navigation of future rovers. Specifically, it focuses on visual odometry (VO) and performs HW/SW codesign to achieve one order of magnitude faster execution and improved accuracy. Conforming to the specifications of the European Space Agency, we built a proof-of-concept system on an HW/SW platform with processing power resembling that to be available onboard future rovers. We developed a codesign methodology adapted to the rover's specifications, design parallel architectures, and customize several feature extraction, matching, and motion estimation algorithms

FUSION: A Full-System Network Co-Simulation Framework

Angelos Athanasiadis[1], Nikolaos Tampouratzis[2], Ioannis Papaefstathiou[1]

Department of Electrical & Computer Engineering, Aristotle University of Thessaloniki, Greece[1]
Department of Industrial Engineering & Management, International Hellenic University, Greece[2]
Email: angelathan@ece.auth.gr; ntampouratzis@ihu.gr; ygp@ece.auth.gr

***Abstract*— Simulating modern distributed systems requires combining accurate software execution with realistic and configurable network behavior, capabilities that no single simulator provides in isolation. This paper presents FUSION, a co-simulation framework that integrates full-system QEMU[1] emulation with OMNeT++ network simulation using the IEEE High-Level Architecture[2] (HLA) standard. Each QEMU instance operates as an independent HLA federate running a complete operating system and unmodified applications, while OMNeT++ models the packet-level network and enforces global time synchronization across all nodes.**

Keywords — Distributed Systems; Distributed Systems Emulation; RISC-V; ARM; QEMU; OMNET++, HLA

I. Introduction

Modern distributed systems, high-performance computing (HPC) and Cloud applications often involve complex interactions between computing nodes and networks. Simulating such systems end-to-end is challenging because no single simulator covers all required components (CPUs, OS, and network) with sufficient detail. Traditional network simulators (e.g., OMNeT++, ns-3) model packet-level communications, while computer architecture simulators or emulators (e.g., gem5, QEMU) simulate full systems capable of running unmodified operating systems and software. Using these in isolation leads to piece by piece evaluation that fails to capture cross-component interactions.

In this paper, we present a co-simulation framework that bridges full-system emulation with network simulation using the High-Level Architecture (HLA) standard. FUSION (Full-System Network Co-Simulation Framework) consists of multiple QEMU instances (emulated nodes) coupled with an OMNeT++ network simulation, all coordinated via an HLA Runtime Infrastructure (RTI). Each QEMU instance runs a standard OS (e.g. Linux) with a virtual network interface card. Instead of connecting directly to a real network, the QEMU network interfaces are intercepted and connected to the OMNeT++ simulation through HLA.

By leveraging HLA for synchronization, we ensure all components share a consistent notion of simulated time, avoiding the timing skew that would occur if we tried to simply run separate emulators in real time. In summary, the main benefits of our approach are:

- **HLA-based QEMU Integration:** A novel integration of QEMU with OMNeT++ via an HLA federation, enabling exchange of real network traffic between emulated OS instances and a network simulator in a time-coordinated fashion.
- **Multi-Node Network Experimentation:** The ability to connect multiple QEMU virtual machines in various topologies (e.g., clusters, IoT networks) by leveraging OMNeT++'s modeling capabilities.
- **Real Software and Stack Execution:** Because QEMU executes real operating systems and applications, our framework can run unmodified software (e.g., Linux with TCP/IP stack, MPI libraries, etc.), obtaining high fidelity in the software behavior.

By combining full-system emulation and network simulation, the tool opens up new opportunities for end-to-end evaluation of distributed systems within a single framework.

II. Related Work

Our work is inspired by the COSSIM framework [1], which interconnects the gem5 simulator with OMNeT++ using IEEE HLA. COSSIM introduced HLA "federation" techniques to link discrete-event network simulation with cycle-accurate processor simulation, overcoming gem5's built-in networking limits. By tapping into gem5's network interface and forwarding packets through an HLA runtime (CERTI), COSSIM enabled multiple gem5 nodes to communicate over arbitrary network topologies defined in OMNeT++. Following a similar philosophy, our framework replaces gem5 with QEMU, a fast full-system emulator. QEMU offers a different accuracy–performance tradeoff, foregoing cycle-level hardware detail for significantly faster execution, while still running real OS and application code. This makes it feasible to simulate larger systems or longer time scales, which is especially useful for HPC scenarios where many nodes and long-running applications are involved.

SimBricks [2] is a modular framework for end-to-end network system evaluation that integrates software and hardware simulators (e.g., QEMU, gem5, Verilator) through a set of standardized simulation bridges. While SimBricks also enables coupling of emulated nodes with network simulation, its architecture requires custom bridges and adapters for each pair of components, which introduces integration complexity. In contrast, FUSION leverages the standardized High-Level Architecture (HLA) interface for time synchronization and message exchange, making it easier to extend or federate with additional simulators.

Authors in [3] present a flexible co-simulation framework (called Virtual Testbed or VTB) for cyber-physical systems, integrating heterogeneous simulators via plugins. In the case study of a modular spacecraft, the authors integrate QEMU to emulate the on-board computer (CPU+FPGA) and use a network SystemC simulator to simulate the SpaceWire network between components.

To the best of the authors' knowledge, no existing framework provides fast full-system emulation with standardized HLA synchronization and OMNeT++ real network modeling.

[1] QEMU is a free and open-source emulator that uses dynamic binary translation to emulate a computer's processor: https://www.qemu.org/

[2] HLA has been developed to provide a common architecture for distributed modeling and simulation: https://standards.ieee.org/ieee/1516/6687/

III. Framework Architecture

Figure 1 illustrates the high-level architecture of the FUSION co-simulation framework. The system consists of multiple processing nodes, each modeled using a full-system QEMU emulator instance running a complete runtime environment (OS, libraries, application). These nodes are interconnected through a network simulator built in OMNeT++, which represents the communication substrate. All components are integrated using the HLA standard: each QEMU instance acts as a separate HLA federate, while the network simulator serves as another federate managing packet-level communication and topology modeling. This setup enables synchronized co-simulation of distributed systems, allowing users to supply custom inputs such as OS images, bootloaders, and application binaries per node, as well as arbitrary network configurations. The framework is extensible to any number of nodes and supports multiple architectures (e.g., ARM, RISC-V).

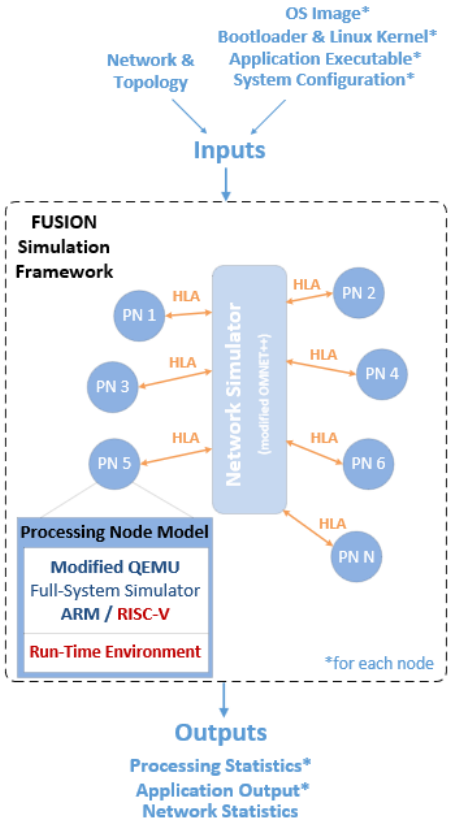

Figure 1: FUSION Simulation Framework

IV. Experimental Results

To demonstrate the performance impact introduced by the proposed co-simulation approach, we conducted a series of experiments using two QEMU-based nodes (ARM and RISC-V) interconnected through our OMNeT++/HLA network model. We used iperf3 [3] to measure end-to-end TCP throughput under a variety of buffer sizes and synchronization intervals. All experiments were performed using identical QEMU configurations and the same virtual NIC (e1000), while varying only the co-simulation parameters.

Figure 2 demonstrates the achieved throughput when varying the application-level buffer size from 1 KB up to 1000 KB, while maintaining a fixed synchronization interval of 1 µs. The results indicate a strong dependency between throughput and offered buffer size. For the ARM node, throughput increases sharply as the buffer rises from small sizes (29.6Mbit/s) towards larger ones (2590Mbit/s). A similar trend is observed for the RISC-V node, with performance ranging from 23.7 Mbit/s (1KB) up to 524Mbit/s (1000KB).

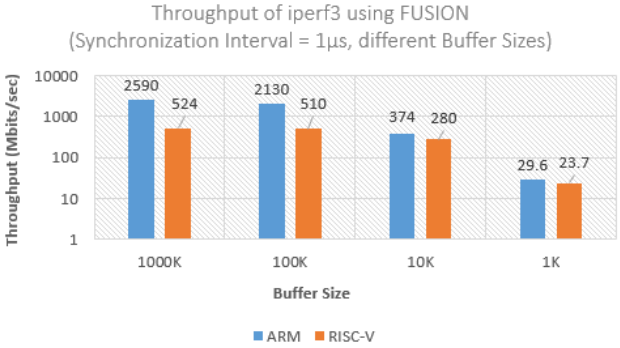

Figure 2: Throughput of iperf3 for different Buffer Sizes

Figure 3 depicts the impact of the synchronization interval in the application throughput (using fixed buffer size). The ARM node achieves a peak throughput of 2600Mbit/s (at 0.1µs), with a gradual drop as the synchronization interval becomes more relaxed. Similarly, the RISC-V node follows the same pattern, ranging from 520 - 553Mbit/s at short interval times (10µs – 0.1µs respectively).

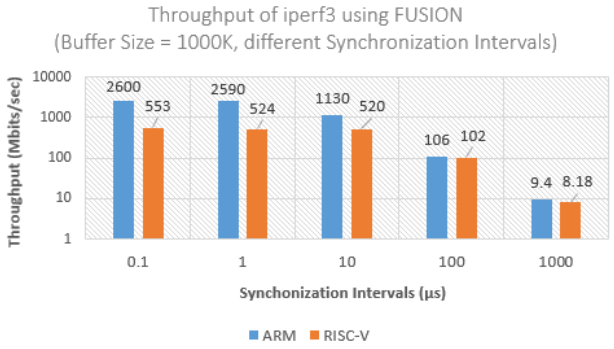

Figure 3: Throughput of iperf3 for different Synchronization Intervals

Overall, the experimental results demonstrate that synchronization granularity introduces a controllable accuracy–performance trade-off. Even at extremely tight synchronization intervals (0.1–1µs), the framework sustains hundreds of Mbit/s on RISC-V and up to 2.6Gbit/s on ARM.

V. Conclusion

In conclusion, we presented FUSION, a co-simulation framework that integrates full-system QEMU emulation with OMNeT++ network simulation through the IEEE HLA standard. Our experimental evaluation validates that HLA-driven synchronization can support realistic multi-node experimentation without compromising determinism.

References

[1] Tampouratzis, N., Papaefstathiou, I., Nikitakis, A., Brokalakis, A., Andrianakis, S., Dollas, A., Marcon, M., Plebani, E.: *A novel, highly integrated simulator for parallel and distributed systems.* ACM Trans. Archit. Code Optim. 17(1) (2020) https://doi.org/10.1145/3378934.

[2] Li, H., Li, J., & Kaufmann, A., *"SimBricks: End-to-End Network System Evaluation with Modular Simulation,"* in Proceedings of the ACM SIGCOMM '22 Conference, Amsterdam, Netherlands, Aug. 22-26, 2022, ACM, New York, NY, USA, pp. 17, https://doi.org/10.1145/3544216.3544253.

[3] J. Reitz, T. Osterloh and J. Roßmann, *"Modeling and Simulation of Cyber-Physical Systems using An Extensible Co-Simulation Framework,"* 2022 Winter Simulation Conference (WSC), Singapore, 2022, pp. 1258-1267, doi: 10.1109/WSC57314.2022.1001

[3] iPerf3 is a tool for active measurements of the maximum achievable bandwidth on IP networks: https://iperf.fr/

Automated Hydroponic Greenhouse for Fodder Production

I.Siakas[1+], D. Triantafyllidis[2]

[1,2] International Hellenic University / Department of Industrial Engineering & Management
P.O. Box 141, 57 400 Sindos, Thessaloniki, Greece

[+] Corresponding author: siakas.ioannis@hotmail.com

***Abstract* — This work presents the design and construction of an automated hydroponic greenhouse for the controlled cultivation of cereal sprouts intended for animal feed. Extended research was conducted, in order to identify the market's needs and the strengths and weaknesses of similar products. The system integrates environmental sensing, irrigation management, air circulation, lighting control, and refrigeration-based climate regulation. Control and monitoring are both performed locally, via a touch-screen Human Machine Interface and remotely through a web-based dashboard. The development emphasized low cost and user-friendly operation. Experimental results demonstrate that environmental conditions can be stabilized despite external disturbances, enabling predictable sprout growth cycles. However, the selection of low-cost structural and electronic components limits reliability and continuous operating capability. The prototype successfully validates the control strategy and overall system architecture, providing a foundation for an improved industrial-grade implementation.**

Keywords — Hydroponics, Greenhouse Automation, Embedded Systems, Environmental Control, Fodder Production.

I. Introduction

Hydroponic cultivation systems for animal fodder enable rapid biomass production in compact, controlled environments. Such systems are particularly relevant where land availability, climatic variability, or logistics restrict conventional agriculture. The goal of this project was to design and construct a compact, automated greenhouse capable of maintaining stable conditions for barley seed germination and sprout development. The system targets low operational cost, ease of use, and remote management, while serving as a platform for further research in controlled-environment agriculture.

II. Research Background

Prior to the design and construction phase, an extended research process was conducted to establish functional requirements and performance constraints for the hydroponic fodder system. This included a study of existing commercial hydroponic units, scientific literature on hydroponic techniques [1-6], and optimal environmental conditions for germination and growth [7-17]. Consultations were carried out with agronomists [18-19] and hydroponic system manufacturers [4] in order to validate cultivation parameters such as humidity level, irrigation frequency, nutrient use, and light exposure. Experimental trials were performed to evaluate the effects of temperature control, airflow distribution, and irrigation timing on sprout uniformity and root mat formation. Additionally, visits to operational hydroponic facilities provided practical insight into construction methods, maintenance considerations, and typical failure modes. The research outcomes directly guided the selection of system components, control strategies, and operational set points implemented in the final prototype.

Fig. 1: Fodder cultivation experiment results.

III. Design Criteria

Based on the findings of the preliminary research phase, a set of design criteria was established to guide the development of the system:

- **Precise Environmental Control:** Maintain stable and optimal temperature, humidity, airflow, irrigation timing, and illumination levels for consistent sprout development.
- **Functional Safety:** Ensure safe operation for both users and equipment through water-level protection, controlled compressor restart logic, electrical safety measures, and integrated fault-detection mechanisms.
- **Intuitive Human–Machine Interaction:** Provide a clear and user-friendly interface that allows system monitoring and parameter configuration without requiring specialized expertise.
- **Remote Supervision and Control:** Enable remote access for real-time monitoring and adjustments via network-connected devices.
- **Energy and Cost Efficiency:** Minimize operational cost by using low-power components, efficient control strategies, and water recirculation to reduce waste.

IV. System Architecture

The greenhouse comprises a steel-frame growth chamber, an air-conditioning unit for temperature and humidity regulation, LED-based lighting, a water reservoir and irrigation system, and an internal air circulation subsystem. The control architecture is distributed across two Arduino microcontrollers communicating via I²C [20]: Controller A (HMI) manages the user interface, data logging, and network communication, while Controller B (Process Control) handles sensor acquisition, actuator control, and closed-loop regulation. Environmental parameters monitored include internal and external temperature and humidity (DHT22 sensors), as well as lighting levels (LDR sensors). Air circulation is provided by a PWM-controlled fan and irrigation is performed through a timed pump–valve sequence with water level feedback from float switches. A web-based dashboard allows real-time monitoring and adjustment of temperature, humidity, lighting intensity, and irrigation intervals.

V. Mechanical Construction

The mechanical structure of the greenhouse was designed and fabricated entirely by the corresponding author, ensuring full control over dimensions, materials, and assembly procedures. The main growth chamber consists of a steel frame constructed from hollow steel profiles, providing rigidity and stability while minimizing weight. The greenhouse features a multi-level design to optimize space usage, with each level supporting trays for seed germination and sprout cultivation. The enclosure is covered with transparent polyethylene film, allowing light penetration while maintaining a controlled environment. The water reservoir is also constructed from metal sheets, securely integrated into the base of the growth chamber to support the irrigation system. Sealing gaskets and silicone were used at joints to ensure water tightness. A separate air-conditioning compartment houses the refrigeration unit and associated ducting. All metallic parts were welded or bolted together, and corrosion protection was applied through painting. The resulting structure combines durability, modularity, and accessibility for maintenance, while serving as a reliable platform for automated environmental control and hydroponic fodder production.

Fig. 2: Automated Hydroponic Greenhouse (front view).

VI. Climate Control

Temperature and humidity are regulated using a refrigeration-based climate control system with independent control of the compressor, evaporator fan, condenser fan, and a four-way reversing valve, enabling both cooling and heating operation. During development, the behavior of a commercial air-conditioning unit was analyzed in order to characterize its operational sequence and replicate

its functionality using an Arduino controller and micro-relays [21]. Four operational modes were implemented (cooling, heating, drying, and standby) to maintain optimal environmental conditions for sprout growth. Additional protective logic was included to limit inrush current during motor startup and to enforce minimum off-time between compressor restarts, thereby preventing mechanical stress and ensuring long-term reliability of the refrigeration system.

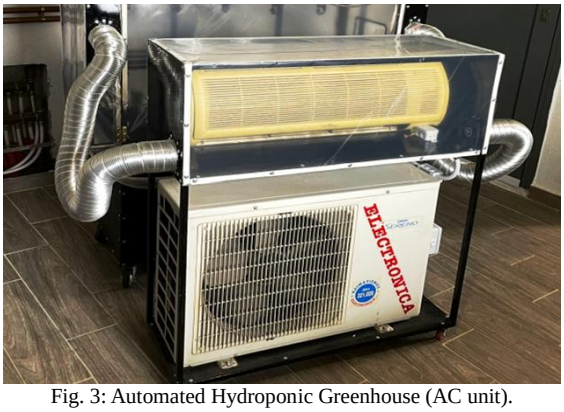

Fig. 3: Automated Hydroponic Greenhouse (AC unit).

VII. Air Circulation

The air circulation subsystem was designed to maintain uniform temperature and humidity distribution within the growth chamber, preventing localized microclimates that could negatively affect sprout development. To determine the optimal placement and geometry of the air inlet and outlet channels, Computational Fluid Dynamics (CFD) simulations were performed using a 3D model of the chamber [22-25]. These simulations evaluated airflow patterns and velocity gradients, enabling the refinement of duct dimensions and diffuser shapes to ensure even air movement across all tray levels. A PWM-controlled axial fan regulates the airflow rate and works in tandem with the climate control system based on feedback from internal temperature and humidity sensors. This closed-loop control approach stabilizes the internal environment, minimizes condensation, and promotes consistent growth conditions throughout the chamber.

VIII. Irrigation Control

The irrigation subsystem is based on a recirculation water tank, which collects the excess water draining from the growth trays and returns it to the system. The tank is equipped with three floating switches that monitor the water level and provide automatic protection against both overflow and dry-running conditions. When the water level falls below the lower threshold, an inlet solenoid valve is activated to refill the tank, while reaching the upper threshold closes the valve to prevent overfilling. An additional top-mounted float switch, wired in normally-closed configuration, acts as an independent failsafe, ensuring that operation is stopped immediately and an alarm is activated in the event of sensor malfunction, cable failure, or valve blockage. This level-based control is a critical safety feature, as it protects the pump and prevents uncontrolled leakage or spillage during continuous operation. Its main advantage over passive water-level regulation techniques is that it provides real-time state feedback to the controller, enabling alarms or secondary safety mechanisms to be triggered in the event of malfunction. Irrigation is delivered through timed cycles, controlled by the microcontroller, using a submersible pump to supply water to misting nozzles that evenly distribute moisture across the growing trays. A manually adjusted flow-splitting regulator is installed in-line to divide the pump output between the misting nozzles and a return loop back to the tank. This mechanical adjustment allows the operator to set the desired spray radius and distribution, compensating for variations in pump characteristics, nozzle clogging, or changes in the number of active nozzles.


Fig. 4: Float switches inside the water tank.

IX. Lighting Control

The lighting subsystem uses full-spectrum LED strips as the primary illumination source, with their brightness regulated through PWM control of the 12V DC supply using a power transistor [26]. To provide accurate feedback for illumination regulation, a custom LDR-based light sensor was designed and calibrated by the author. The calibration process involved simultaneous sampling of the sensor's output voltage and reference lux measurements taken with a standardized light meter (UNI-T UT383). Based on these

measurements, a logarithmic correlation function was derived to map the sensor's digital readings to real illumination values in lux, and this function was integrated directly into the Arduino control code. A PID controller [27] uses the calibrated light measurements to adjust the PWM duty cycle in real time, maintaining a constant target illumination level throughout the growth cycle. This closed-loop regulation ensures stable photosynthetically active radiation (PAR) at the plant surface, regardless of external lighting conditions, LED aging, or power supply variation, promoting uniform sprout development and improving overall energy efficiency.

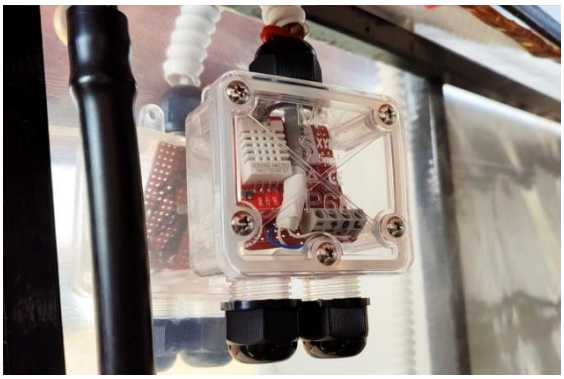

Fig. 5: Environmental sensors module.

X. Electronics And Wiring

All electronic components are housed within a dedicated control enclosure to ensure safe operation and ease of maintenance. Power distribution separates high-voltage AC circuits from low-voltage DC circuits to minimize interference and electrical hazards. Appropriate MCBs and fuses are used to protect wiring and sensitive electronic devices. Cable selection (including cross-section, type, and color coding) follows the EN 60204-1 [28] standard to ensure compliance and safety. All wiring is routed using protective conduits and sealing materials to maintain enclosure tightness and a dedicated safety circuit has been implemented to prevent unintended or unsafe system behavior. Labeled DIN rail terminal blocks facilitate assembly, troubleshooting, and replacement of components. Signal lines for sensors and PWM-controlled actuators are routed with shielding where necessary to reduce electromagnetic interference and ensure reliable operation. Cable routing is secured and organized to prevent mechanical stress, accidental disconnections, or exposure to moisture, ensuring long-term safety and reliability of the greenhouse control system.

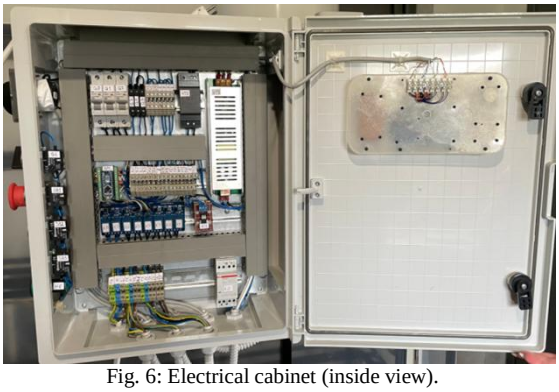

Fig. 6: Electrical cabinet (inside view).

XI. Arduino Programming

The control software was developed using the Arduino IDE [29] and is distributed across two microcontrollers that communicate via the I²C protocol. The first controller handles sensor acquisition, actuator control, and closed-loop regulation of the climate, irrigation, and lighting subsystems, while the second controller manages the local human–machine interface and remote communication. The program is structured as a state machine, where each operating mode of the system is represented as a discrete state with defined transitions. This approach ensures deterministic behavior, simplifies debugging, and prevents conflicting commands by guaranteeing that only the actions of the active state are executed at any time. Non-blocking timing routines based on internal millisecond counters were used instead of delay functions, allowing all subsystems to operate concurrently without interrupting control loops. Modular programming practices were applied throughout, with separate functions for sensor reading, PID regulation, safety interlocks, timed events, and user interface updates. This architecture enhances reliability, improves code maintainability and provides a scalable foundation for future expansion of system capabilities.

XII. Local User Interface

The system incorporates a local human–machine interface designed to provide clear and intuitive operation. A touch-screen display with a color graphical interface and three status LEDs allow the user to view real-time sensor readings, adjust system parameters, select operating modes, and initiate irrigation or climate control functions without requiring prior technical knowledge. The interface layout and menu structure were designed to be simple and logically organized, minimizing the risk of operator error. In addition to the touch

display, dedicated physical controls are included for essential safety and manual override functions. These consist of selector switches for operating mode selection, push-buttons for starting/stopping operation, and an emergency stop “mushroom” button that immediately disables all power outputs in case of malfunction or unsafe conditions. This combination of digital and physical controls ensures both ease of use during normal operation and secure, controlled intervention during troubleshooting or emergency scenarios.

XIII. Remote User Interface

The system provides remote monitoring and control via a network-connected interface [30], enabling operators to access the greenhouse from any compatible device. Real-time environmental data, including temperature, humidity, light intensity, and irrigation status, are transmitted through WiFi with an ESP-01 module using ATtention commands. Data are sent to a remote SQL data base, which acts as an intermediary between the Arduino controller and the web interface, allowing bidirectional communication for sending commands and receiving sensor readings. Users can adjust set points and operating schedules remotely. This remote capability enhances operational efficiency and ensures consistent cultivation conditions even when direct on-site supervision is not possible.

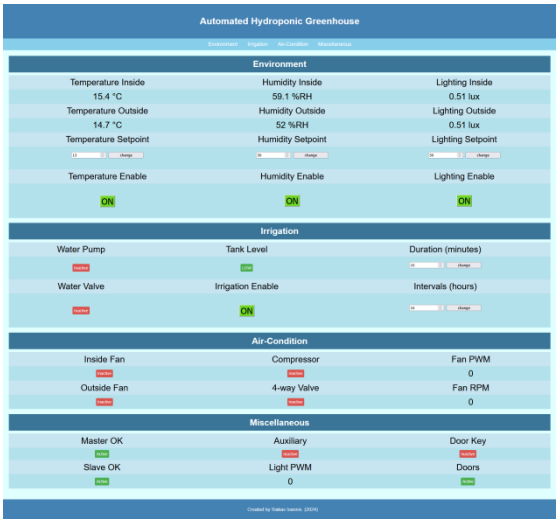

Fig. 7: Remote supervision and control website.

XIV. Results

Barley sprouts developed consistently and reached harvestable stage within the expected time window. However, several reliability limitations were identified:

- Low-cost HVAC compressor and fan components resulted in slow thermal response.
- The transparent polyethylene film that was used to cover the chambers, did not provide adequate insulation.
- Arduino control boards exhibited intermittent faults during extended operation.

These issues do not affect the validity of the control approach but limit continuous industrial operation.

XV. Conclusions And Future Work

The prototype successfully demonstrates automated controlled-environment hydroponic cultivation for fodder production. The control algorithms, local and remote user interfaces and remote monitoring framework all functioned as intended. To advance toward an industrial-grade system, future development should focus on replacing low-cost components with standardized, industrial-grade hardware, enhancing sealing and corrosion resistance, integrating fault detection and system health monitoring, and implementing data-driven optimization of climate and irrigation profiles. Additionally, the user interface could be refined to meet industrial standards, and features such as data logging and historical trend visualization could be incorporated to support performance analysis and optimization of growth cycles. With the increasing availability of artificial intelligence, neural networks and machine learning algorithms could be employed to provide optimization suggestions or even automatically adjust environmental parameters based on feedback from each production cycle. This work establishes a solid foundation for a scalable and reliable hydroponic fodder production platform.

References

[1] Alagro, Αυτοματισμός υδροπονικών εγκαταστάσεων, http://www.alagro.gr/

[2] BIOstalis, Υδροπονική καλλιέργεια ζωοτροφής, https://www.biostalis.com/

[3] D. Smart, Μονάδα υδροπονικής καλλιέργειας ζωοτροφής,https://www.dnasmart.gr/hydroponic_forage.html

[4] E. F. Solutions, Υδροπονικοί θάλαμοι ζωοτροφής, https://emma.gr/ta-proionta-mas/pure-fodder/

[5] Αεροπονική, Προϊόντα εσωτερικής καλλιέργειας, https://aeroponic.gr/

[6] Γαίας Έργον, Ολοκληρωμένο σύστημα υδροπονίας,https://www.gaiasergon.gr/services/cultivationtechnologies/hydroponics-system/

[7] W. F. Gericke, "Hydroponics: The growing of plants without soil," California Agricultural Experiment Station Circular, vol. 29, pp. 1–10, 1929.

[8] W. F. Gericke, "A new way of growing plants without soil," Journal of the American Society for Horticultural Science, vol. 38, pp. 1–7, 1933.

[9] W. F. Gericke, The Complete Guide to Hydroponics. McGraw-Hill, 1936.

[10] NASA, "Hydroponic fodder systems for space missions," NASA, Tech. Rep., 2018. [Online]. Available:https://ntrs.nasa.gov/api/citations/20180005362/downloads/20180005362.pdf.

[11] NASA, "A novel approach to growing gardens in space," NASA Science, 2022. [Online]. Available: https://science.nasa.gov/science-research/science-enabling-technology/technologyhighlights/a-novel-approach-to-growing-gardens-in-space/

[12] Αριστοτέλειο Πανεπιστήμιο Θεσσαλονίκης, Υδροπονικές καλλιέργειες, https://www.aua.gr/ekk/archives/334

[13] Wikifarmer.com, Hydroponics articles and resources,https://wikifarmer.com/library/en/tag/hydroponics

[14] Syngenta, Καταπολέμησε τις ασθένειες στα σιτηρά, https://www.syngenta.gr/nea/stohorafi/katapolemise-tis-astheneies-sta-sitira

[15] Meteofarm, Η καλλιέργεια του κριθαριού, https://www.meteofarm.gr/μμ/

[16] Yara, Στάδια ανάπτυξης του κριθαριού, https://www.yara.gr/threpsh-kalliergeiwn/kalliergiakritharіou/stadia-anaptyksis-krithari/

[17] Yara, Λίπανση κριθαριού, https://www.yara.gr/threpsh-kalliergeiwn/kalliergia-krithariou/

[18] Γ. Παλάτος, Καθηγητής γεωπονίας, ΔΙΠΑΕ, http://giorgos-palatos.blogspot.com/2010/10/blogpost.html

[19] Β. Ασχονίτης, Εντεταλμένος ερευνητής, ελγο-δημητρα, https://www.swri.gr/index.php/el/component/sppagebuilder/page/93

[20] Wikipedia Contributors, IIC, https://en.wikipedia.org/wiki/I2C

[21] Δημήτρης Τερτίπης, "Ψυκτικοί κύκλοι," Αριστοτέλειο Πανεπιστήμιο Θεσσαλονίκης, Tech. Rep., 2015.[Online]. Available: https://eclass.uowm.gr/modules/document/file.php/MECH261/Chapter_11.pdf

[22] F. Community, Freecad: Open source 3d parametric modeler, https://www.freecad.org/

[23] O. Foundation, Cfmesh: Automated mesh generation for openfoam, https://cfmesh.com/

[24] O. Foundation, Openfoam: The open source cfd toolbox, https://openfoam.org/

[25] I. Kitware, Paraview: Open source scientific visualization, https://www.paraview.org/

[26] Arduino, Basics of pwm (pulse width modulation), https://www.arduino.cc/en/Tutorial/PWM

[27] Wikipedia Contributors, PID controller,https://en.wikipedia.org/wiki/Proportional%E2%80%93integral%E2%80%93derivative_controller

[28] iTeh, En 60204-1:2018 - safety of machinery - electrical equipment of machines - part 1: General requirements, 2018. [Online]. Available: https://standards.iteh.ai/catalog/standards/clc/d77744c9-9b58-4018-a6c2-894686047f7a/en-60204-1-2018

[29] Arduino. *arduino-ide v2.3.6 Release* [Software]. GitHub. Available: https://github.com/arduino/arduino-ide/releases/tag/2.3.6

[30] I. Siakas, *ArduinoGreenhouse Project Website* [Online]. Available: http://arduinogreenhouse.atwebpages.com/

Electronically Controlled Distillation Chamber with Integrated IoT System

Dimitrios Ouzounis[1], Kyriakos Tsiakmakis[1], Maria S. Papadopoulou[1], Vasileios D. Vassios[1], Konstantinos A. Tsintotas[1], Argyrios T. Hatzopoulos[1]

[1] Department of Information and Electronic Engineering
International Hellenic University
57400 Sindos, Thessaloniki, GREECE
Corresponding email: ahatz@ihu.gr

***Abstract*—Progress in the field of electronics has led to the use of automation and IoT technologies in traditional processes, such as pharmaceutical distillation, essential oil production and alcoholic solutions. This paper presents the design and implementation of an electronic control system for a distillation chamber and the live visualization of process parameters on remote devices. The central control unit utilizes a Raspberry Pi 4 and the values of critical operating parameters are recorded on a Node.js/MySQL server to achieve remote monitoring and control, ensuring accuracy, safety and optimization of distillate production. The system is low-cost, features a local unit for full operation and enables remote control using IoT technologies. Measurements during system operation demonstrated satisfactory accuracy and verified the control of the overall process.**

KeyWords— Distillation system, electronic circuit, embedded, IoT, low cost, Raspberry Pi 4, remote devices, sensor

I. INTRODUCTION

The process of distillation is one of the oldest chemical separation techniques, with the first recordings dating back to ancient Mesopotamia [1]. Despite its long history, the fundamental principle remains the same: the separation of various components based on the difference in their boiling points, which is achieved through boiling at different temperatures, evaporation of components, and subsequent condensation. In most small-scale units, temperature monitoring and heating regulation are still performed using analog indicators and simple manual control. This methodology leads to measurements of reduced accuracy and negatively impacts the quality of the final product.

This work addresses the need for high-accuracy measurements, which are crucial in the distillation process [2]. Furthermore, the system is designed to provide easy local operation through a user-friendly interface and to enable the user to record the entire process and monitor it remotely for reliable execution according to desired specifications. This is achieved by using Cloud and IoT technologies via the Raspberry Pi 4. Finally, the system tries to maintain a low budget and ease of use. The final evaluation of the system demonstrated success in achieving these objectives.

II. SYSTEM ARCHITECTURE

A. System Overview

The system is composed of heating and cooling tanks, sensors, and electronic control elements (Fig. 1). Specifically, it consists of the following main components: Central Control Unit, Raw Material Boiling Tank (Boiling Chamber), Heating System controlled by the central unit, and a Cooling Chamber with a pump. A block diagram representation is shown in figure 2.

Figure. 1. Photo of the distillation system.

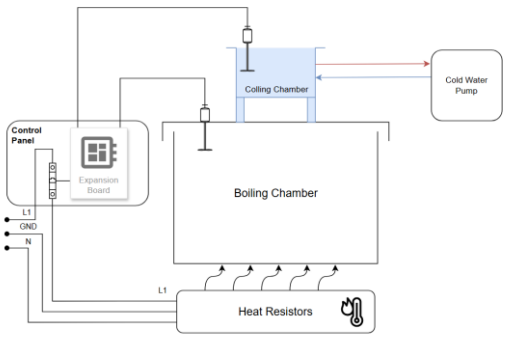

Figure. 2. Block diagram of the system

B. *Central Control Unit*

The central control unit is the core of the embedded system. It receives commands from the user, displays measurements and system status, controls the operation and transmits necessary information to a cloud database.

The main processing and control unit consists of a Raspberry Pi 4 Model B (RPi4) and a custom made expansion board that connects it to sensors, control buttons, display and the relay controlling the heating element. All electronic subsystems are integrated into a plastic enclosure suitable for industrial use with an IP55 protection rating. The same enclosure also serves as the physical user interface.

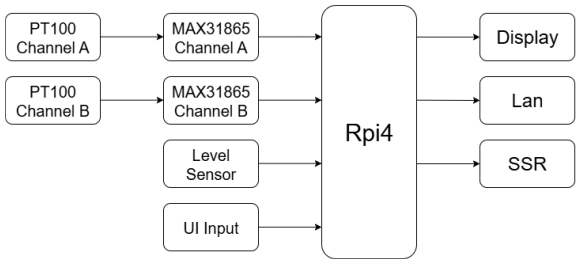

Figure 3. Control unit's block diagram

Figure 4. Control unit's front panel and interior

The software managing both the hardware operation and the application logic is developed in Python, enabling programmed control of peripherals, data collection and storage and interconnection with the user application. Table 1 lists the devices connected to the RPi4.

TABLE 1. DEVICES CONNECTED TO RASPBERRY PI 4

Component	Function
Expansion Board	Custom PCB for connections
PT100 Sensor (3-wire)	Temperature measurement
Rotary Encoder	Setpoint adjustment/User input
Solid State Relay (16A)	Heating element control
LCD Display	Local data visualization
Emergency Button	Immediate system shutdown

C. *Raw material boiling tank and cooling chamber*

The distillation tanks of essential oils and alcoholic beverages play a decisive role in the final result. They are mainly made of stainless steel, due to their resistance to corrosion and their properties that do not alter the final product.

For the present work, a domestic use distillation device was used and is made of stainless steel. It is an economical and reliable choice for experimenting with various distillation techniques, with accuracy, quality and ease of handling. To monitor the temperature, PT100 temperature sensors were placed in a suitable case.

The cooling chamber was implemented with a container made of stainless steel, a copper coil and a PT100 temperature sensor. To maintain the desired condensation temperature, there was a pump circulating cold water.

D. *Temperature Measurement Subsystem*

For the correct and reliable measurement of temperature, PT100 temperature sensors were used. For their operation in this system, the use of a circuit with low offset voltage amplifiers, high input impedance and large CMRR, adjustable gain and implemented with a unipolar power supply is required [4].

For convenience, instead of implementing a sensor conditioning circuit with discrete components, the integrated component MAX31865 from Maxim Integrated, was used, which integrates the necessary amplifying devices, electrical signal filters, a signal linearization stage, a signal conversion unit from analog to digital and a communication unit in the SPI protocol (Fig. 5).

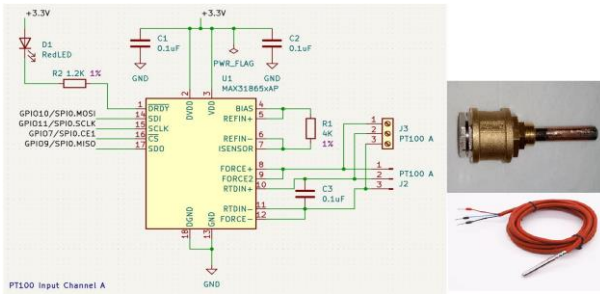

Figure 5. Temperature measurement subsystem with PT100 temperature sensor in a case

E. *Heating Subsystem*

A common household electric hotplate providing a stable and controlled thermal power of 2200 Watts was used for heating the boiler. Its selection was based on ease of use and low cost. The control of the heating element is achieved by the Rpi4 using a Solid State Relay (SSR) 16A. The Rpi4 software controlled the operation of the arrangement according to the user's selections.

III. CONTROL SYSTEM AND CLOUD COMMUNICATION

The main processor (Raspberry Pi 4) executes a Python application that integrates the required libraries: MAX31865 (adafruit_max31865), I/O and GPIO handling (board, digitalio, gpiozero), LCD display control (RPLCD.i2c), and real-time communication (python-socket). In addition, supporting modules are employed for peripheral device management and application functionality on the Raspberry Pi 4, such as threading for concurrent task execution and schedule for timed task automation. These modules ensure efficient resource utilization and reliable system operation.

Following system initialization, the application establishes a WebSocket connection with the server to enable bidirectional data and command exchange.

Thereafter, the LCD display, the emergency button state, the water level sensor, and the corresponding indicators on the user interface are initialized, ensuring proper synchronization between hardware components and the application environment.

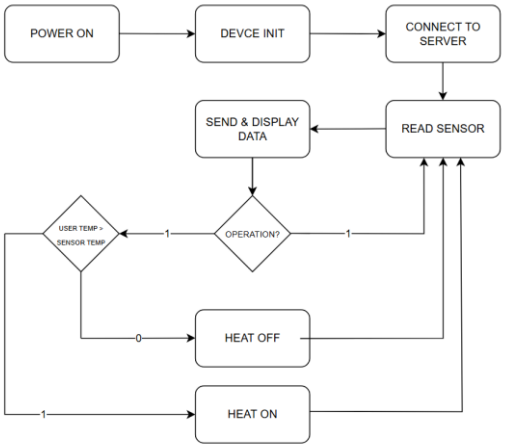

Figure 6. Simplified algorithm's flow chart

Once the setup is complete, the system begins operation. Measurements are acquired and transmitted to a remote computer hosting the server. The server processes and stores all data, providing remote monitoring and full control of system functions through the user application. The user application incorporates embedded JavaScript code, which facilitates dynamic interaction, real-time updates, and responsive visualization of system states, thereby enhancing usability and overall system efficiency.

Figure 7. Remote use interface

The server and user application were implemented in JavaScript using the Node.js framework. The Node.js server leverages Google's V8 engine to execute code outside the browser. A MySQL relational database was employed to reliably store the recorded measurements and system information.

IV. EXPERIMENTAL RESULTS

To evaluate the system's function, a distillation process was performed using 1 L of water as the initial raw material. During operation, critical parameters such as temperature change rate, measurement accuracy and data visualization were observed. The experimental setup included three sensors positioned at critical points: one PT100 sensor (Channel A) in the condenser tank, one PT100 sensor (Channel B) installed in the boiler cap to monitor the vapor temperature, and a handheld infrared thermometer to verify the cooling tank temperature.

The process lasted 3 hours, 26 minutes and 32 seconds. After completion, 0.6 L of pure distillate were collected, while 0.3 L remained in the boiler. The remaining 0.1 L corresponded to losses and residual volume in the condenser's coil.

Based on the analysis of measurements, the maximum temperature in the boiler successfully reached the boiling point of water, confirming the efficient heating and steam production.

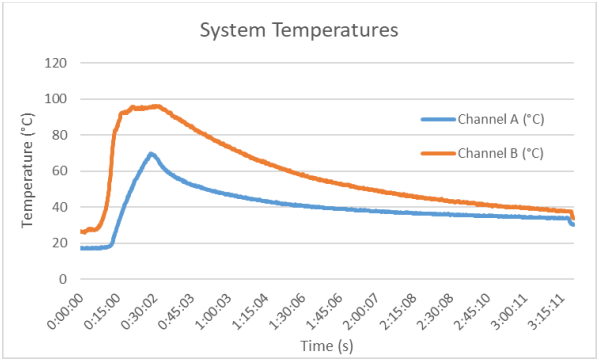

Figure 8. Temperature in the boiler (A) and in the condenser tank (B)

Conversely, the average temperature in the condenser remained significantly lower, indicating that the cooling procedure and the steam condensation were effective.

Finally, the comparison of the PT100 sensor temperature with the handheld thermometer revealed a very deviation (<1°C) which is an acceptable value, because the PT100 measures inside the cooling tank. Also, the system successfully regulated the operating temperature according to the user's selections and the data transmission, storage and real-time visualization were successfully achieved.

V. CONCLUSIONS

The system successfully achieved the objective of creating an electronically controlled distillation chamber. The embedded solution based on the RPi 4, coupled with high-accuracy PT100 sensors and custom signal conditioning, proved effective in precisely regulating the heating element via the SSR. The system successfully regulates operating parameters, transmits and stores data in a MySQL database via the Node.js server, and visualizes the process in real-time through a web

interface, thus meeting the criteria for a modern IoT control system. The final evaluation showed a low measurement deviation, confirming system's reliability.

VI. REFERENCES

[1] N. Kockmann, "History of distillation," in Elsevier eBooks, 2014, pp. 1–43. doi: 10.1016/b978-0-12-386547-2.00001-6.

[2] F. A. Kalbani and J. Zhang, "Inferential Composition Control of a Distillation Column Using Active Disturbance Rejection Control with Soft Sensors," Sensors, vol. 23, no. 2, p. 1019, Jan. 2023, doi: 10.3390/s23021019.

[3] A. M. H. Al-Ani et al., "Implementation of Real-Time Edge Computing on Raspberry Pi 4 for AI Applications," IEEE Access, vol. 9, pp. 130327-130338, 2021, doi: 10.1109/ ACCESS.2021.3113115.

[4] A. T. Hatzopoulos, K. Tsiakmakis, V. Delimaras, F. T. Stoupas, V. D. Vassios, and M. S. Papadopoulou, "Automated Controlled Chamber for Measuring Plant Growth," International Review of Electrical Engineering (IREE), vol. 18, no. 4, pp. 254–263, 2023, doi: 10.15866/iree.v18i4.23731

[5] Maxim Integrated Products, Inc., "RTD-to-Digital Converter," MAX31865 datasheet, Nov. 2015.

Measuring the resonance frequency and attenuation of Polyvinylidene Fluoride (PVDF) beams

Ippokratis Kochliaridis
Industrial Eng. and Management
International Hellenic University, Greee
ippokoch@iem.ihu.gr

Michail E. Kiziroglou
Industrial Eng. and Management
International Hellenic University, Greee
m.kiziroglou@imperial.ac.uk

***Abstract*— Acoustic Power Transfer (APT) is a type of electro acoustical system. Especially, it is a modern type of interface where data signals and power supply are transmitted with the use of mechanical waves in a medium. An APT system usually contains piezoelectric transducers with ultrasound frequency response, as elements for the transmitter and the receiver part. This paper describes the evaluation of a measuring arrangement which contains an APT receiver. The receiver consists of 4 piezoelectric sensors made from PVDF material. Different masses were installed in each element edge to obtain different resonant frequencies. Due to the different masses, each beam possesses a unique resonant frequency, at which point it functions as a mechanical filter. To determine these resonant frequencies, theoretical models of the damped response had to be compared with the measured data. The resonant frequency in the first piezoelectric element noticed at 53 Hz ± 1 Hz, with a damping coefficient 33 sec^{-1} ± 2 sec^{-1}. The resonance frequency in the second transducer, noticed at 16 Hz ± 1 Hz, with damping coefficient 10 sec^{-1} ± 1 sec^{-1}.**

Keywords—Acoustic Power of Transfer, Mechanical Waves, Vibrations, Piezoelectric Transducer, Wireless Charging

I. THEORETICAL BACKGROUND

Acoustic Power Transfer (APT) is a novel type of wireless interface based on mechanical waves. APT systems could have a wide range of applications, such as boats, aircrafts, automotive and biomedical devices [1-2]. An APT system is an electroacoustic system which typically consists of an acoustic source, a medium of transfer, and a receiver (Fig. 1), where most of these systems utilize piezoelectric transducers with frequency response up to 1 MHz [3-4]. On the transmitter side, a driver uses the piezoelectric effect to generate acoustic waves from electrical power, the receiver then converts acoustic waves into electrical power again. The medium of transfer could be air, water, metal and even a tissue [1]. However, utilizing a single transducer for both transmission and reception, it results in low power efficiency and the data rate is limited up to 55 kbps [2]. To achieve high power efficiency, array techniques with multiple piezoelectric elements have been employed on both the transmitter and receiver sides. Especially, more than 17 Mbps were achieved with a pair of piezoelectric discs [5] and up to 700 Mbps using a combination of seven emitters and seven receivers [6]. However, the operational modes of typical piezoelectric sensors are not optimized for the resonant frequency region and they are primarily designed to exhibit a flat frequency response, as conventional arrays are primary intended for measurements. As a result, it is challenging for conventional piezoelectric arrays to supply adequate power and stable voltage to remote devices, such as aircraft sensors embedded within a metallic chassis. Therefore, an experimental receiver comprising four piezoelectric sensors was evaluated (Fig. 2). Each element is composed of a PVDF beam with an attached tip mass, where these cantilevers are installed above a metallic surface. Due to the different masses, each beam possesses a unique resonant frequency, at which point it functions as a mechanical filter. To determine these resonant frequencies, theoretical models of the damping response had to be compared with the measured data. This paper is organized as follows:

- Part II presents the mathematical concept of a damping response.
- Part III describes the evaluation of electroacoustic measurements.
- Part IV analyses the results of measure data.
- And Part V is potential future research.

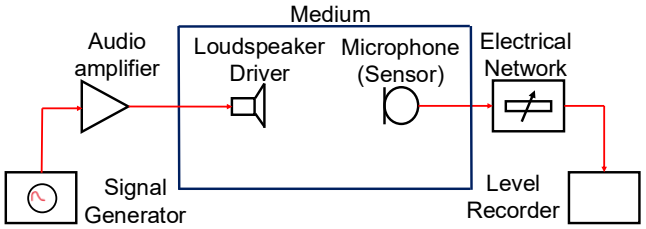

Fig. 1: The block diagram of a speaker driver's frequency response measurement is considered a simplified APT system.

II. MATHEMATIC MODEL

A damped sine wave or damped sinusoid is a sinusoidal function whose amplitude approaches zero as time increases. It corresponds to the *underdamped* case of damped second-order systems, or underdamped second-order differential equations [7]. Damped sine waves are commonly seen in science and engineering, wherever a harmonic oscillator is losing energy faster than it is being supplied. A true sine wave starting at time = 0 begins at the origin (amplitude = 0). A cosine wave begins at its maximum value due to its phase difference from the sine wave. A given sinusoidal waveform may be of intermediate phase, having both sine and cosine components. The term "damped sine wave" describes all such damped waveforms, whatever their initial phase.

The most common form of damping, which is usually assumed, is the form found in linear systems. This form is exponential damping, in which the outer envelope of the successive peaks is an exponential decay curve. That is, when the maximum points of each successive curve are connected, the result resembles an exponential decay function. The general equation for an exponentially damped sinusoid may be represented as [8]:

$$y(t) = Ae^{-\lambda t}cos(\omega t - \varphi) \quad (1)$$

Where $y(t)$ is the instantaneous amplitude at time t, A is the initial amplitude of the envelope, λ, is the decay rate, in the reciprocal of the time units of the independent variable t, φ is the phase angle at $t = 0$, ω is the angular frequency. In addition, a damped waveform in order to be designed properly, other parameters that should be considered are the *frequency*, *time constant*, *half-life, damping ratio* and *Q-factor*. The frequency is expressed as: $f = \omega/2\pi$ which is the number of cycles per time unit. It is expressed in inverse time units t^{-1}or *Hz*. Time constant $\tau = 1/\lambda$ is the time for the amplitude to decrease by the factor of *e*. Half-life is the time it takes for the exponential amplitude envelope to decrease by a factor of 2. It is equal to $ln(2)/\lambda$ which is approximately $0.693/\lambda$. Damping ratio ζ is a non-dimensional characterization of the decay rate relative to the frequency, approximately $\zeta = \lambda/\omega$ or exactly $\zeta = \lambda/\sqrt{\lambda^2 + \omega^2}$ <1. Finally, Q-Factor is expressed as $Q = 1/(2\zeta)$ which is another non-dimensional characterization of the amount of damping, high Q indicates slow damping relative to oscillation.

III. Materials and Methods

In order to measure piezoelectric sensors at specific resonance frequencies, some experiments were evaluated. The acoustical measurements were evaluated in the Microelectromechanical Systems Laboratory of the Department of Industrial Engineering and Management, IHU. The measuring setup was composed of a Siglent SDS1102CML+ digital oscilloscope, an aluminum rectangular plate and a custom array construction from piezoelectric cantilevers. The oscilloscope supports up to 100 MHz bandwidth (-3 dB), 1 GSa/s sampling rate and two channels with BNC connectors [9]. For the APT experiments, an aluminum rectangular surface was chosen of 1 m by 1 m and a thickness of 4 mm. The metallic surface was placed on a laboratory workbench, with four stands located at the plate corners. The stands are 100 mm length and contain rubber washers as sound absorber elements, in order to minimize unwanted vibrations and noise sources to the receiver.

A receiver array was evaluated with four piezoelectric elements. Each sensor was a flexible cantilever beam made of a PVDF material. Different masses were installed in each element edge to obtain different resonant frequencies. The 100 Vibration Sensor from Measurement Specialties [10], was chosen for the array construction. According to the datasheet, the sensor provides 1.1 V/g voltage sensitivity (open-circuit, baseline) and 260 pC/g charge sensitivity. In addition, the resonance frequency is 75 Hz and the inertial mass is at 0.3 g. Fig. 2, shows a photograph of this installation above the metal plate.

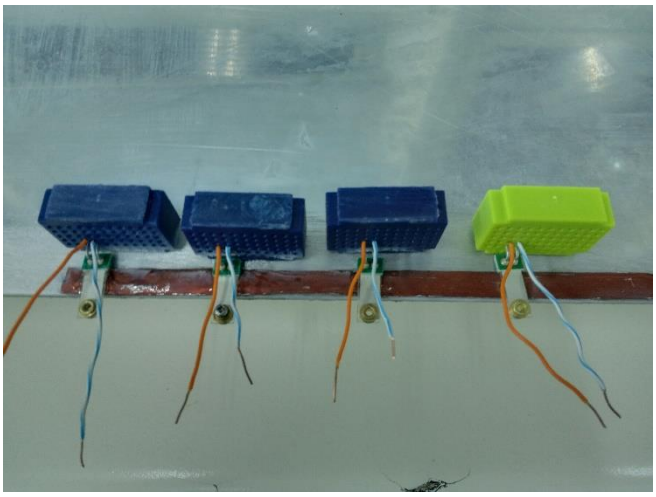

Fig. 2: Photograph of the receiver setup (Each sensor element without any mass installation).

Transducer response was measured under steady-state excitation when applied a harmonic point force in the aluminum rectangular surface. Mechanical waves were radiated, when applied an impulse force manually in the system's input using an impact hammer. Fig. 3 represents a block diagram's construction of this measure arrangement.

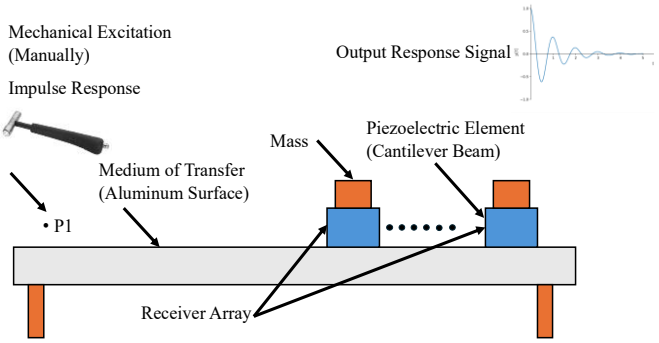

Fig. 3: Block diagram of the measurement system-side view**.** This diagram illustrates the setup including the acoustic medium (aluminum surface) and the receiver, which consists of two piezoelectric cantilever beams.

IV. Experimental Study

Fig. 4 illustrates the damping response waveform (mathematical model) compared to the measured data for the first two piezoelectric sensors from the experimental array. Top graph is the damping response of the first piezoelectric sensor without an attached mass and the bottom graph illustrates a piezoelectric sensor with an attached mass (two neodymium magnets, 38 g). The resonant frequency in the first piezoelectric element noticed at 53 Hz ± 1 Hz, with a damping coefficient 33 sec^{-1} ± 2 sec^{-1}. The resonance frequency in the second transducer, noticed at 16 Hz ± 1 Hz, with damping coefficient 10 sec^{-1} ± 1 sec^{-1}. The agreement on both waveforms is very good (bolt black line represents the mathematical model prediction and red line represents the measure data).

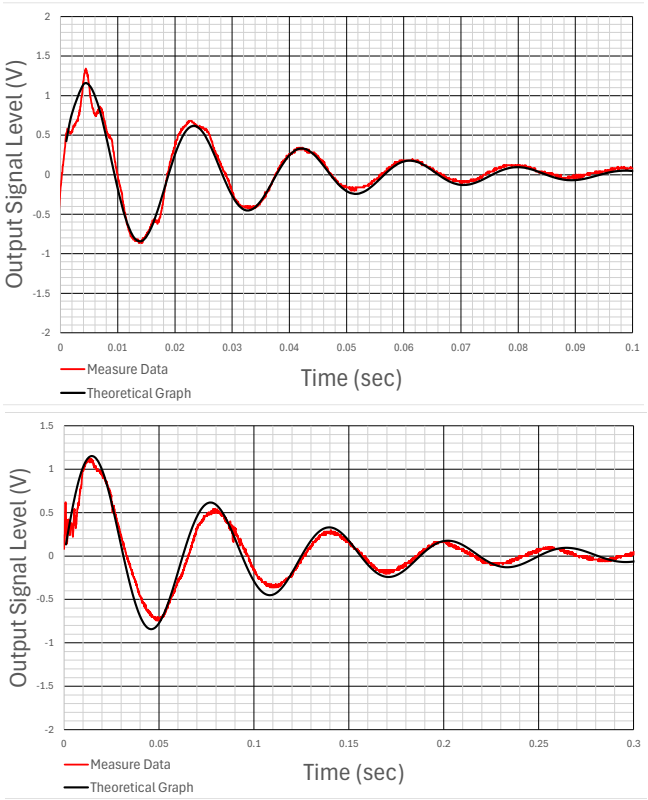

Fig. 4: Array damping response. (Top) The damping waveform signal of the first piezoelectric sensor. (Bottom) The damping waveform signal of the second piezoelectric sensor. In both panels, the bold black line represents the mathematical model prediction, and the red line represents the measured experimental data.

V. Further Research

The next step of research would be a prediction of vibrations dispersions and acoustic power levels across a rectangular metallic surface. As result, a software like COMSOL could be used. Fig. 5 illustrates a 3D view of an electroacoustic system from the project and Fig. 6 shows the geometry mesh. The 3D drawing contains an indicative part of a large rectangular metallic surface. Also includes a piezoelectric beam (the small rectangular cantilever) an acoustic source and air domain, which is the outer rectangular. Every surface of the model contains variable/parameters from the proper materials.

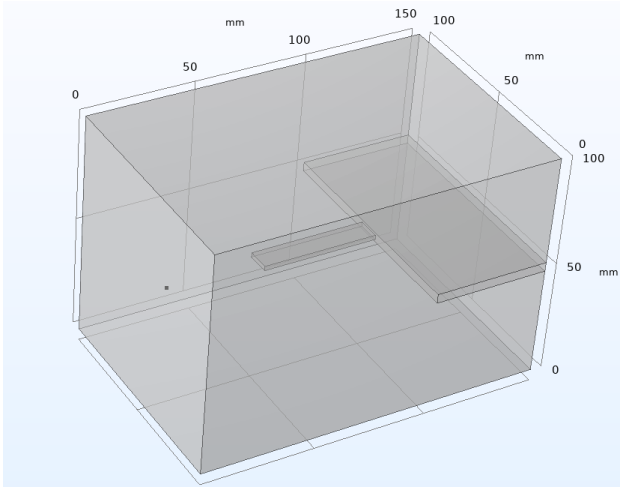

Fig. 5: 3D view of the model.

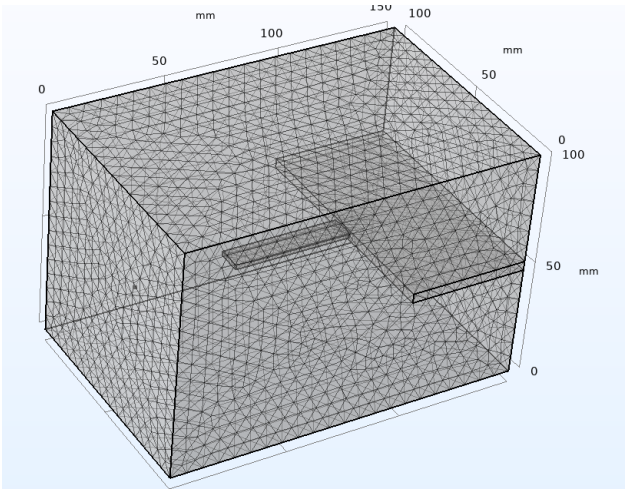

Fig. 6: Mesh illustration of the 3D geometry.

Acknowledgement

This paper was created for the 10th International Workshop on Microsystems, Alexander Campus, International Hellenic University, 08 December 2025.

References

[1] Lee, Sung Q., Woosub Youm, and Gunn Hwang. "Biocompatible wireless power transferring based on ultrasonic resonance devices." *Proceedings of Meetings on Acoustics*. Vol. 19. No. 1. Acoustical Society of America, 2013..

[2] Freychet, O., et al. "Analytical optimization of piezoelectric acoustic power transfer systems." *Engineering Research Express* 2.4 (2020): 045022.

[3] Yang, Hengxu, et al. "An ultrasonic through-metal-wall power transfer system with regulated DC output." *Applied Sciences* 8.5 (2018): 692.

[4] Recommendations and Reports of the CCIR,*ITU, Volume_XIII*_(Last_Access:18/11/2025) https://search.itu.int/history/HistoryDigitalCollectionDocLibrary/4.282.43.en.1018.pdf

[5] Lawry, Tristan J., et al. "A high-performance ultrasonic system for the simultaneous transmission of data and power through solid metal barriers." *IEEE transactions on ultrasonics, ferroelectrics, and frequency control* 60.1 (2012): 194-203.

[6] Ashdown, Jonathan D., et al. "High-rate ultrasonic through-wall communications using MIMO-OFDM." *IEEE Transactions on Communications* 66.8 (2018): 3381-3393.

[7] Douglas C. Giancoli (2000). [*Physics for Scientists and Engineers with Modern Physics (3rd Edition)*]. Prentice Hall. p. 387 ISBN 0-13-021517-1.

[8] https://en.wikipedia.org/wiki/Damping.

[9] Siglent Dual Channel Digital Oscilloscope (Datasheet-Last_access:18/11/25) https://www.siglent.eu/product/1139189/siglent-sds1102cml-100mhz-dual-channel-oscilloscope.

[10] MiniSense Cantilever-PVDF type vibration sensor (Datasheet-Last-Access:18/11/2025) https://files.seeedstudio.com/wiki/Piezo-Sensor---MiniSense-100/res/MiniSense_100.pdf.

A Camera-based Portable Scattering Analyser Towards Blood Cell Photoplethysmography

Eleni Kapetangiorgi and Michail E. Kiziroglou
Department of Industrial Engineering & Management, International Hellenic University

***Abstract*—A portable light scattering analyser system is presented, based on a laser source and a camera chip. It can provide dynamic light scattering measurements from blood samples as well as from light transmission through thin tissues. Results using latex sphere buffers corresponding to the sizes of red blood cells, white blood cells and platelets indicate that Mie scattering profiles can potentially be detected, allowing correlation to cell size and concentration. In combination with other techniques, the proposed portable scattering analysis platform could provide a new non-invasive method for blood cell plethysmography.**

Keywords—blood cell, Mie scattering, photoplethysmography.

I. Introduction

The goal of this paper is to make known the results of experiments, related to assembling a sensor and using it as a tool to measure light scattering, caused by the components of blood, as well as to correlate the measured scattering with the constituents' morphological characteristics, in hopes of contributing to the scientific research for the invention of non-invasive portable biomedical sensors [1, 2].

In earlier research on the subject [1, 2], the component used to capture the scattering phenomenon was a linear Photo Diode Array (PDA), whereas in this paper a camera chip was utilised for the same purpose. PDAs can provide much faster response, with framerates exceeding 1000 samples per second. On the other hand, cameras provide higher resolution in pixels per unit length, and a symmetric circular measurement for each angle which can be used for improved position calibration and averaging. Another advantage is that they are available at very low-cost and high-end specifications, because they are supported by the very broad commercial camera industry.

The layout of the sensor, with which the experiments were done, consists of three key electronic parts: a light source, a digital camera and a microcontroller platform. The light travels from the source to the sample, it gets scattered and then captured by the camera. The pixel data is sent to a computer through the microprocessor, where it's finally saved and analysed, as represented in figure 1.

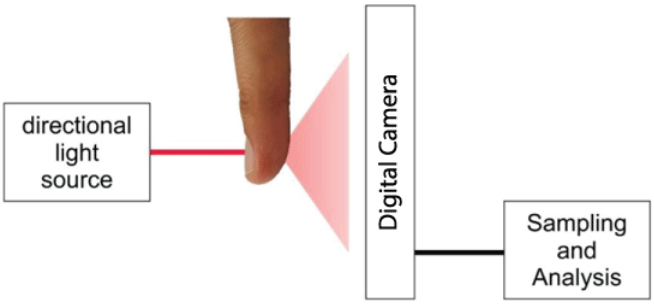

Fig. 1. Schematic representation of the measuring process [2].

II. Sensor Hardware

More specifically, the parts listed in the previous paragraph are: a laser pointer generating red-coloured light, the OV7670 camera by Omnivision and a microprocessing platform compatible with Arduino's Uno model. Shown in Figure 2, while in use, all of the above are laid out on top of objects with a hard surface, in a way that each one of them is in the position needed to allow the light scattering capture.

For the needs of these particular experiments, the QVGA resolution (160 x 120 px) and the YUV 4:2:2 colour profile were selected, between the multiple image capturing settings available on the OV7670. This combination allows the generation of photographs with sufficient quality for analysis and small enough memory usage, suitable for fast data transfer and save, at the same time.

Fig. 2. Layout of the sensor, while in operation.

III. Sensor Software

The sensor's capturing and analysing process, from beginning to end, is handled by three separate custom scripts, executed as a sequence.

In order of execution, the first one is responsible for the operation of the microprocessor, including its communication and data exchange with the digital camera. The next script's purpose is to send the captured image data from the microprocessor to the computer, so it can be saved, in both image and text format. The third and last one is where the saved pixel data is processed. The direction, together with the intensity of the scattered light, get visualised into a plot for optical comparison and extraction of conclusions.

IV. Experiment Results

The developed scattering analysis system was used to perform a series of experiments using nanosphere solution buffers with diameters corresponding to the size of red (4.8 μm) and white (9.6 μm) blood cells as well as platelets (2 μm). Indicative captured images are shown in Fig. 3. These results were analysed to obtain the light intensity profile as a function of scattering angle, in order to investigate whether a Mie scattering profile can be detected. For this purpose, the brightness across a linear interval aligned to the centre of the detected light spot was plotted and studied. Indicative results are presented in Fig. 4, Fig. 5 and Fig. 6. A steep contrast

between the main light spot and dark areas is clearly depicted. The rising and falling light intensity profiles show remarkable symmetry and demonstrate a slope reduction, at around half the maximum intensity. This is evident between brightness levels 90 and 150 in Figure 4, for the 2 μm diameter spheres (corresponding to platelets). The effect is more pronounced in the case of Figure 5, around the same brightness levels, for the 4.8 μm diameter spheres (corresponding to red blood cells). In Figure 6, this effect is weaker, but there is an intensity increase at the edges resulting in two lobes in the profile for 9.6 μm spheres (corresponding to white blood cells).

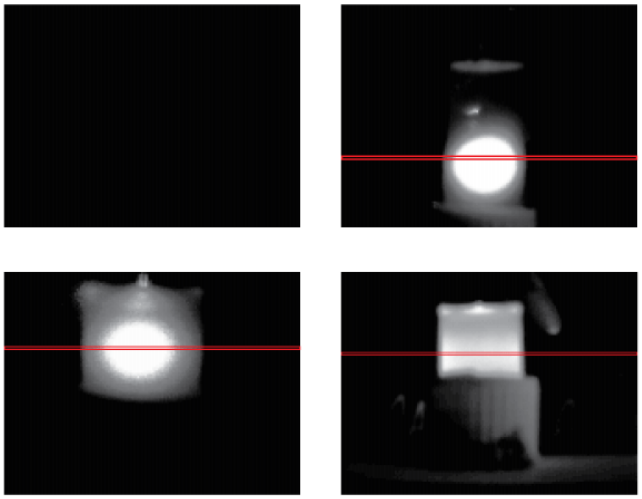

Fig. 3. Examples of samples taken, with the analysed line of pixels highlighted.

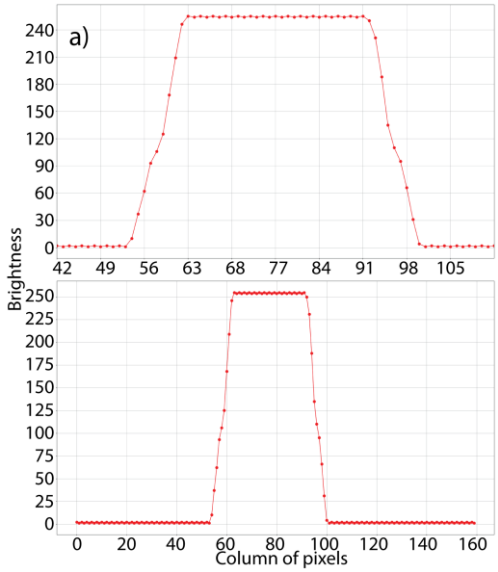

Fig. 4. Linear profile measurements from the images of Fig. 3, with light intensity measured in brightness arbitrary units, from a 2 μm microsphere solution corresponding to platelets.

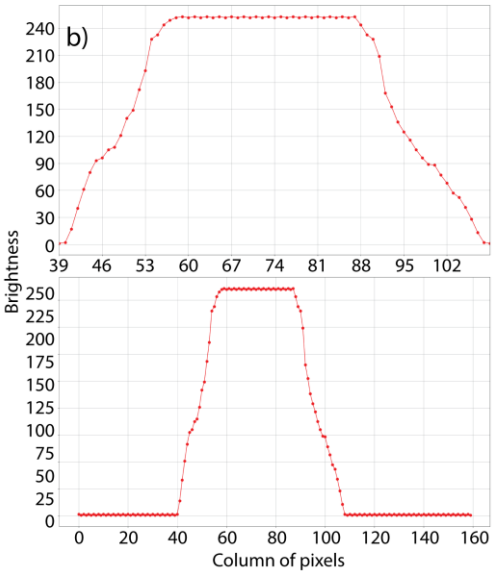

Fig. 5. Linear profile measurements from the images of Fig. 3, with light intensity measured in brightness arbitrary units, from a 4.8 μm microsphere solution corresponding to red blood cells.

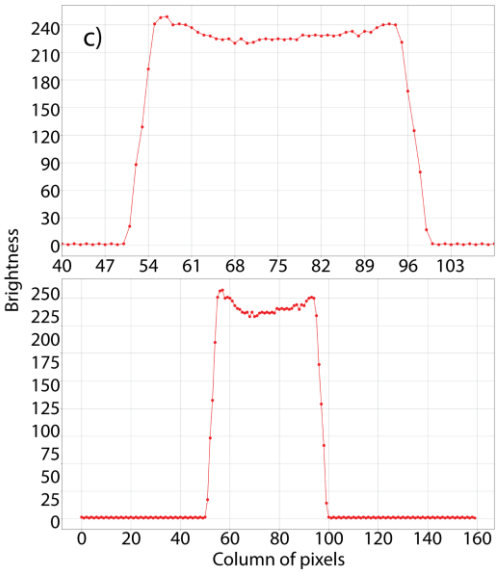

Fig. 6. Linear profile measurements from the images of Fig. 3, with light intensity measured in brightness arbitrary units, from a 9.6 μm microsphere solution corresponding to white blood cells.

V. Conclusions

A camera-based light scattering analysis system was developed for in-vitro and in-vivo measurements of light scattering on blood cells. The results indicate light intensity slope variations at laser spot edges. These variations show promise for correlation with Mie scattering profiles, that can be reinforced, by additional measurements on baseline samples or others of different consistency, in the future. The combination of this system with other techniques such as light polarisation to minimise multiple scattering signal, confocal microscopy, pulse-based differential measurements, spectroscopic analysis and occlusion [3-5] could lead to a non-invasive blood cell plethysmography technology.

References

[1] K. Karakostas *et al.*, "Blood cell size determination by scattering analysis," in *2019 Panhellenic Conference on Electronics & Telecommunications (PACET)*, 2019, pp. 1-5.

[2] K. Karakostas, S. Gkagkanis, K. Katsaliaki, P. Köllensperger, A. Hatzopoulos, and M. E. Kiziroglou, "Portable optical blood scattering sensor,"

Microelectronic Engineering, vol. 217, p. 111129, 2019/09/15/ 2019.

[3] J. M. Goldman, M. T. Petterson, R. J. Kopotic, and S. J. Barker, "Masimo signal extraction pulse oximetry," (in eng), *J Clin Monit Comput*, vol. 16, no. 7, pp. 475-83, 2000.

[4] Z. Lu, X. Chen, Z. Dong, Z. Zhao, and X. Zhang, "A Prototype of Reflection Pulse Oximeter Designed for Mobile Healthcare," *IEEE Journal of Biomedical and Health Informatics*, vol. 20, no. 5, pp. 1309-1320, 2016.

[5] I. Fine and A. Finarov, "Probe for use in non-invasive measurements of blood related parameters," ed: Google Patents, 2006.

Aircraft Structural Health Multi-Sensor Wireless Node Powered by Energy Harvesting

Jaime G. Alonso[1], Robin Berguerand[2], Adrien Candelotto[3], Alexis Carriere[3], Philippe Dallemagne[2], Andrew S. Holmes[4], Daniel Iniesta[1], Michail E. Kiziroglou[4,5] *, David Marty[3], Damien Piguet[2], Steven W. Wright[4] and Eric M. Yeatman[4,6]

[1]Airbus Defence and Space, SPAIN, [2] CSEM, SWITZERLAND, [3]Serma Ingenierie, FRANCE,

[4]Imperial College London, UNITED KINGDOM, [5]International Hellenic University, GREECE and [6]University of Glasgow, UNITED KINGDOM

In this work, a wireless multi-sensor node is designed for aircraft structural monitoring. It is powered by an inductive energy harvesting power supply developed for non-invasive coupling to aircraft power lines. The sensing performance is evaluated and the energy autonomy is studied in various scenarios involving different data acquisition and transmission modes including cold starting. Indicatively, regulated continuous power of 13 mW is provided from a 10 A RMS, 500 Hz line current, with 10 min cold-starting time and 2.3 J energy buffer. This supports the sensor node maximum power of 40 mW during 200 Hz strain data acquisition, at a duty cycle of over 40%.

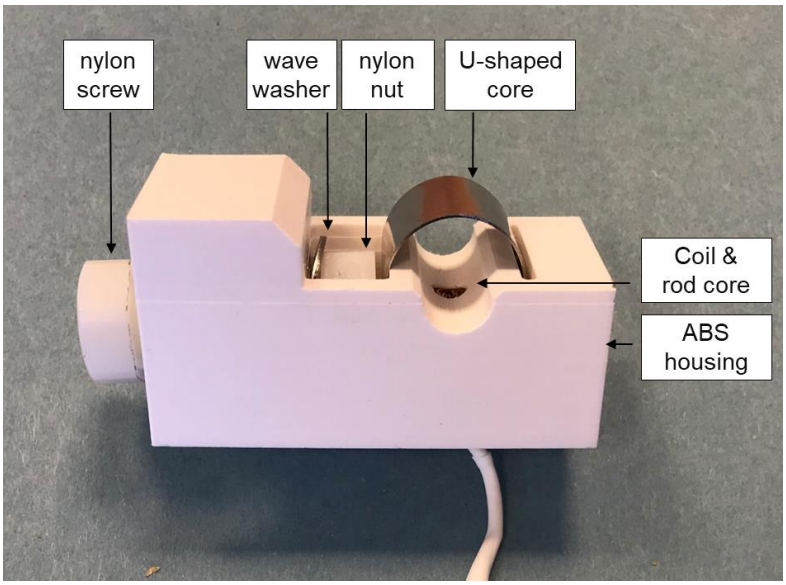

Figure 1. Photo of the power line harvester.

References

[1] Wright et al, "Inductive Power Line Harvester With Flux Guidance for Self-Powered Sensors," IEEE Sensors Journal, 23 (18), 20474, 2023.

[2] Kiziroglou et al, "Dual Storage Power Management for Energy Autonomous Microsystems," IEEE Transactions on Industrial Electronics, 72 (8), 8657, 2025

Building a Safer Future with Olympia Electronics

Abstract: The development and production of advanced security systems is a discipline that requires unwavering dedication and a strong sense of responsibility toward people and property.
At Olympia Electronics, we combine expertise with innovation. Our Research & Development and Production departments operate with precision, applying rigorous quality controls at every stage of the process.
Leveraging state-of-the-art technologies, including fully automated SMD production lines, we ensure flawless assembly of electronic boards—delivering products that meet the highest standards of reliability, safety, and performance.

In this talk, an overview of the activities and products of Olympia Electronics in the field of Safety and Security Systems will be presented. Our Product Portfolio:

- Emergency Lighting – Featuring LiFePO4 battery technology and supercapacitor solutions for enhanced durability and efficiency.
- Fire Detection & Extinguishing Systems – Advanced detectors and intelligent control panels for comprehensive fire safety.
- Thermostats – Precision-engineered for optimal environmental control.
- Access Control Systems – Secure, scalable solutions for modern facilities.

Analysis of Operational Deviations and Their Implications for the Steady-State Assumption in Small-Scale R134a Refrigeration Cycles

Aliyara Aubakirova[1] and Dimitrios Tziourtzioumis[2] [0000−0002−1881−3953]

[1]Department of Civil Engineering, University of Messina
[2] Laboratory of Energy Systems, Department of Industrial Engineering and Management, International Hellenic University, Alexander University Campus, 57400 Sindos, Greece
aliyara.aubakirova@studenti.unime.it

***Abstract*— The accurate performance evaluation of vapor-compression refrigeration systems is predicated on the fundamental assumption of steady-state operation. This study presents a critical analysis of experimental data from an R134a system, where standard thermodynamic calculations yielded a physically impossible negative Coefficient of Performance (COP). A systematic diagnostic methodology, involving first-law analysis and pressure-enthalpy (P-h) diagram mapping, was employed to investigate the anomaly. The results identified a violation of the isenthalpic expansion principle, where the enthalpy after the expansion valve (h4) exceeded the enthalpy after the condenser (h3), and a significant inconsistency in the compressor's mechanical-electrical coupling, evidenced by a decrease in torque concurrent with an increase in current. These findings conclusively demonstrate that the system was operating in a faulty, non-steady-state condition, likely due to a compound failure involving the compressor and expansion valve. This case study underscores the critical necessity of pre-processing data validation in experimental thermodynamics to prevent misapplication of steady-state models. A diagnostic checklist is proposed to verify thermodynamic coherence and operational stability prior to performance calculation, thereby enhancing the reliability of experimental analysis and fault diagnosis in refrigeration systems.**

Keywords — Refrigeration Cycle, Coefficient Performance (COP), Data Validation

I. INTRODUCTION

The accurate performance evaluation of vapor-compression refrigeration systems fundamentally relies on the assumption of steady-state operation. In this study, the operational stability and thermodynamic coherence of an R134a refrigeration system are critically analyzed using experimental data that exhibit significant anomalies. Since the uncritical application of steady state models to transient or faulty system behavior can lead to physically impossible results and profound diagnostic errors, a rigorous assessment of operational data is essential. In this work, first-law thermodynamic analysis and pressure-enthalpy (P-h) diagram mapping are employed to diagnose the system state. The coefficient of performance (COP), compressor work, and enthalpy values across the cycle were calculated from the measured data. The results, including a negative COP and violations of the isenthalpic expansion principle, indicate a severe departure from expected steady-state behavior. A diagnostic framework is proposed to validate data coherence prior to performance calculation. The findings demonstrate that the proposed diagnostic checklist can successfully identify non-steady-state and faulty operations from thermodynamic data. This methodology can be employed to prevent misinterpretation of experimental results, thereby improving the reliability of system performance analysis and aiding in the accurate diagnosis of technical malfunctions.

II. THEORETICAL FRAMEWORK

The theoretical foundation of this analysis rests on the established principles of thermodynamics and the standard vapor-compression refrigeration cycle. This framework provides the benchmark for ideal system behavior, against which the experimental data from the R134a system is compared to identify and diagnose anomalies.

A. The Standard Vapor-Compression Refrigeration Cycle

The vapor-compression cycle is the fundamental model for analyzing refrigeration systems, as comprehensively detailed in foundational thermodynamics texts like Çengel & Boles (2015). The cycle consists of four key processes, illustrated on a Pressure-Enthalpy (P-h) diagram, which is the most useful tool for refrigeration analysis:

1. Isentropic Compression (Process 1–2): The refrigerant, entering the compressor as a saturated or superheated vapor at state 1, is compressed to a high pressure and temperature (state 2). This process requires work input, W_in = m_dot * (h2 - h1).
2. Isobaric Condensation (Process 2–3): The high-pressure vapor rejects heat to the surroundings in the condenser, first de-superheating and then condensing into a liquid at state 3.
3. Isenthalpic Expansion (Process 3–4): The high-pressure liquid passes through an expansion valve (or capillary tube), where its pressure and temperature drop rapidly. This process is modeled as isenthalpic, meaning h3 = h4 (Stoecker & Jones, 1982).
4. Isobaric Evaporation (Process 4–1): The low-pressure mixture of liquid and vapor absorbs heat (the desired cooling effect) in the evaporator, transforming completely into a vapor

before returning to the compressor at state 1. The cooling capacity is Q_in = m_dot * (h1 - h4).

The primary performance metric derived from this cycle is the Coefficient of Performance (COP), defined as the ratio of the desired heat removal to the required work input: COP = Q_in / W_in = (h1 - h4) / (h2 - h1) By definition, for a functioning refrigeration system, Q_in > 0 and W_in > 0, resulting in a COP > 0.

B. The Steady-State Assumption in Experimental Practice

The validity of the standard cycle analysis is predicated on the system operating at a steady state. As outlined in testing standards like ANSI/ASHRAE Standard 37 (2009), a steady state is achieved when all system parameters (temperatures, pressures, flow rates, and power consumption) remain constant within a narrow band over a sufficient period. This assumption allows for simplification of the governing equations by eliminating time-dependent terms. However, as discussed by Bendapudi & Braun (2002), real systems are inherently dynamic, and the attainment of a true steady state is an idealization. Control system interactions, component hysteresis, and latent faults can prevent this, leading to the collection of data that does not represent a coherent thermodynamic state.

C. Fault Signatures and Thermodynamic Coherence

When a system deviates from steady-state operation due to a fault, its thermodynamic state points will no longer conform to the ideal cycle. The field of Fault Detection and Diagnosis (FDD) has catalogued how specific failures manifest in system data (Kim et al., 2019; Breuker & Braun, 1998). Key fault signatures relevant to this study include:

• Compressor Faults: Failure of reed valves or internal leakage, as described by Breuker & Braun (1998), leads to reduced compression efficiency, manifested as a lower discharge temperature (t2) and a discrepancy between the electrical power input and the fluid work output (h2-h1). This can explain anomalous torque and current readings.

• Expansion Device Faults: A malfunctioning expansion valve, often "hunting" for stability as analyzed in control studies like Elliott & Rasmussen (2010), violates the isenthalpic assumption. This results in a measurable difference between h3 and h4, disrupting the entire energy balance.

• Refrigerant Charge Issues: Both undercharge and overcharge, as well as the presence of non-condensable gases, create pressure-temperature relationships that deviate from the pure refrigerant properties found in the ASHRAE Handbook (2020).

A "thermodynamically coherent" data set is one where all measured and derived properties are consistent with the First Law of Thermodynamics and the expected state relationships of the working fluid. Plotting the state points on a P-h diagram for R134a provides a powerful visual test for this coherence. Data from a stable, well-functioning system will form a closed, logical cycle. Data from a faulty or transient system will not.

By applying this multi-faceted theoretical framework—combining the ideal cycle model, the critical importance of the steady-state assumption, and known fault signatures—the subsequent analysis will deconstruct the anomalous data from the R134a experiment, demonstrating a clear case where the underlying assumptions of standard performance evaluation were invalid.

III. Case Study: Analysis of an Anomalous R134a Refrigeration System

This case study centers on the experimental investigation of a small-scale refrigeration unit using R134a as the working fluid. The primary data, as previously outlined, was collected over two short duration runs and exhibited significant inconsistencies that preclude standard performance evaluation. 1. System Description and Data Collection The experimental setup consisted of a standard vapor-compression cycle comprising a hermetic compressor, a condenser, an expansion valve, and an evaporator. Key operational parameters were measured, including:

• Electrical & Mechanical: Rotational speed (RPM), voltage (V), current (A), and torque (τ).

• Thermodynamic State: Pressures (P1-P4) and temperatures (t1-t4) at the compressor inlet (1), compressor outlet (2), condenser outlet (3), and evaporator inlet (4). The derived parameters, specifically the mass flow rate (m_dot) and specific enthalpies (h1-h4) at each state point, were calculated using the measured data and the thermodynamic properties of R134a, as tabulated in the ASHRAE Handbook Fundamentals (2020).

2. Identification of Anomalies through Thermodynamic Analysis The standard vapor-compression cycle model, as defined by Çengel & Boles (2015), provides the basis for identifying the following critical anomalies.

Deviation 1: The Physically Impossible Coefficient of Performance (COP)

The Coefficient of Performance is the primary metric for refrigeration efficiency, calculated as: COP = Q_in / W_in (1) Where:

• Cooling Capacity, Q_in = m_dot * (h1 - h4) (2)

• Compressor Work Input, W_in = m_dot * (h2 - h1) (3) Using the reported data:

• For Run 1: COP = 1032.7 kJ/h / 1106.6 kJ/h = -0.93

• For Run 2: COP = 887.2 kJ/h / 581.4 kJ/h = -1.53

A negative COP is thermodynamically impossible for a refrigeration cycle, as it implies the system is producing a cooling effect while generating work, which violates the Second Law. This is the most significant indicator that the system was not in a viable steady state or that the data is fundamentally flawed (Kim et al., 2019).

Deviation 2: Violation of the Isenthalpic Expansion Principle

A cornerstone of the standard cycle model is that the expansion across the valve is isenthalpic (Stoecker & Jones, 1982). This requires: h3 = h4 (4) However, the reported data shows:

• Run 1: h3 = 259.02 kJ/kg, h4 = 272.22 kJ/kg → Δh = +13.2 kJ/kg

• Run 2: h3 = 259.20 kJ/kg, h4 = 271.40 kJ/kg → Δh = +12.2 kJ/kg

This consistent and significant positive enthalpy difference

(h4 > h3) indicates a clear violation of the model's fundamental assumptions. This could be caused by a severely malfunctioning expansion valve, significant heat transfer to the expansion device, or erroneous sensor readings at states 3 or 4 (Elliott & Rasmussen, 2010).

Deviation 3: Incoherent Cycle Representation on a P-h Diagram

When the reported state points are plotted on a P-h diagram for R134a, they fail to form a closed, logical cycle. The process lines do not follow the expected paths: the "compression" process (1- 2) does not follow a line of increasing entropy, and the "expansion" process (3-4) is not vertical (isenthalpic). This visual incoherence is a direct result of the data not representing a true thermodynamic equilibrium state, a common issue when systems are in transient operation or have underlying faults (Bendapudi & Braun, 2002).

Deviation 4: Inconsistent Mechanical-Electrical Coupling

The relationship between mechanical power and electrical power provides insight into the compressor's health. The mechanical power can be calculated as: $W_{mech} = (2 * \pi * RPM * \tau) / 60$ (5)

For Run 1: $W_{mech} = (2 * \pi * 1053 * 9.4) / 60 \approx 1038$ W

For Run 2: $W_{mech} = (2 * \pi * 1050 * 8.1) / 60 \approx 891$ W

The electrical power input is: $W_{elec} = V * I$ (6)

For Run 1: $W_{elec} = 70$ V * 16 A = 1120 W

For Run 2: $W_{elec} = 70$ V * 17 A = 1190 W

The discrepancy between the mechanical power calculated from torque and the electrical power input, coupled with the decrease in torque alongside an increase in current, is a classic signature of a compressor's fault. This suggests internal damage, such as broken reed valves, causing inefficient compression and increased motor effort, as documented in FDD literature (Breuker & Braun, 1998).

3. Diagnostic Conclusion

The convergence of these four anomalies—the impossible negative COP, the violation of isenthalpic expansion, the incoherent P-h diagram, and the aberrant compressor performance— leads to a single, robust conclusion: the refrigeration system was undergoing a significant technical malfunction during the data collection period.

The most probable root cause is a compound fault: a failure of the compressor's internal valve, potentially induced or exacerbated by a malfunctioning expansion valve. This fault combination would create a positive feedback loop of instability, preventing the system from ever reaching the steady-state condition required for valid performance analysis as per standards like ANSI/ASHRAE Standard 37 (2009). This case study therefore serves as a critical example of the pitfalls of applying steady-state models to a system in a faulty, non-equilibrium state.

IV. Conclusion

This study presented a critical analysis of operational data from an R134a refrigeration system, where the application of standard thermodynamic models yielded physically impossible results, most notably a negative Coefficient of Performance (COP). Through a systematic investigation grounded in the principles of the vapor-compression cycle and fault detection methodologies, it was conclusively demonstrated that the system never achieved a steady-state operating condition. The root cause was identified as a likely compound failure, involving a mechanical fault within the compressor—evidenced by an inverse relationship between torque and current— coupled with a malfunctioning expansion valve, indicated by the violation of the fundamental isenthalpic expansion principle. The case study underscores a critical, often overlooked, aspect of experimental thermodynamics: the steady-state assumption is a prerequisite, not a guarantee. Applying performance evaluation models to data from a system in distress or transient operation leads not merely to inaccuracies, but to thermodynamic impossibilities that invalidate the results. This analysis serves as a stark reminder that rigorous data validation must precede advanced calculations.

To mitigate such issues, this work proposes the adoption of a pre-processing diagnostic checklist, including stability criteria, physical plausibility checks, and cycle coherence tests using P-h diagrams. By implementing such protocols, researchers and engineers can safeguard the integrity of their analyses, ensure the accurate diagnosis of system faults, and uphold the reliability of experimental performance data. Future work should focus on developing automated, real-time data validation tools and conducting intentional fault implantation studies to further refine these diagnostic frameworks for next-generation refrigeration systems.

References

[1] ANSI/ASHRAE Standard 37-2009. Methods of Testing for Rating Electrically Driven Unitary Air-Conditioning and Heat Pump Equipment. American Society of Heating, Refrigerating and Air-Conditioning Engineers, Atlanta, GA (2009).

[2] ASHRAE Handbook. Fundamentals. American Society of Heating, Refrigerating and AirConditioning Engineers, Atlanta, GA (2020).

[3] Bendapudi, S. & Braun, J. E. A review of literature on dynamic models of vapor compression equipment. ASHRAE Transactions 108, 1–25 (2002). 4. Breuker, M. S. & Braun, J. E. Common faults and their impacts for rooftop air conditioners. HVAC&R Research

[4] 303–318. https://doi.org/10.1080/10789669.1998.10391406 (1998).

[5] Çengel, Y. A. & Boles, M. A. Thermodynamics: An Engineering Approach (8th ed.). McGraw-Hill Education, New York (2015).

[6] Elliott, M. S. & Rasmussen, B. P. On reducing evaporator superheat nonlinearity with control architecture. International Journal of Refrigeration 33, 607–614. https://doi.org/10.1016/j.ijrefrig.2009.12.012 (2010).

[7] Kim, M., Kim, M. S. & Chung, J. D. A review of fault detection and diagnosis methods for refrigeration and air conditioning systems. International Journal of Refrigeration 106, 1– 21. https://doi.org/10.1016/j.ijrefrig.2019.07.006 (2019).

[8] Stoecker, W. F. & Jones, J. W. Refrigeration and Air Conditioning (2nd ed.). McGraw-Hill, New York (1982).

An Online Framework for Quality Control, Anomaly Detection and Auto-Calibration of Hourly Air-Quality Data from an IoT Sensor Node

Minas D., Tsiakmakis K., Hatzopoulos, A.T., Papadopoulou M. and Vassios V.

Department of Information and Electronic Engineering
International Hellenic University, Sindos, Thessaloniki, Greece

Abstract— This work presents an end-to-end pipeline designed to improve the quality and trustworthiness of hourly air-quality data collected by a multi-sensor IoT node. The node measures temperature, relative humidity, particulate matter (PM2.5 and PM10), carbon monoxide (CO), carbon dioxide (CO2), nitrogen oxides (NO, NO2) and UV index on a university campus. A Python backend streams the measurements into a database and drives a web dashboard that runs rule-based quality control (QC), multivariate anomaly detection, time-series analysis and short-term forecasting in near real time.

The system operates in two complementary modes. In online mode, the incoming hourly stream is continuously analyzed and visualized with QC flags, anomaly markers, daily statistics, intraday profiles and 24-hour-ahead forecasts. In offline mode**, the same tools are applied to a complete stored period, together with a robust, data-driven auto-calibration step that targets spikes, heavy anomalies and small gaps in the sensor signals by replacing only clearly abnormal samples with median-based estimates that are consistent with the typical behavior of the node.**

A month-long pilot deployment demonstrates that the proposed approach substantially reduces the impact of rare but severe anomalies on PM2.5 statistics while preserving the underlying diurnal pattern. The overall workflow is lightweight, transparent and well suited both for small-scale deployments that require reliable air-quality information and for educational environments where students can interact with live data, explore anomalies and directly observe their effect on statistics, forecasts and decision support.

Index Terms— Environmental monitoring, IoT sensors, anomaly detection, quality control, auto-calibration, data cleaning.

I. Introduction

Environmental sensor nodes have become an attractive option for smart cities, campuses and citizen science initiatives, because they provide dense spatial coverage of key air-quality indicators at a fraction of the cost of regulatory stations. However, the resulting data streams are often affected by noise, calibration drift, missing values, communication issues and occasional extreme outliers. If we don't deal with these effects in a careful, structured way, they can give us the wrong picture of how much pollution there really is and make our analytics and forecasting models work much worse than they should. Recent work has highlighted the importance of anomaly detection and repairing of air-quality data, to improve the reliability of monitoring systems and downstream analyses [1]. At the same time, several studies have focused on the design of sensing infrastructures and IoT-based air-quality stations that can be deployed in urban environments and integrated with cloud or fog-computing platforms [2], [3]. Other contributions have analyzed the behavior of air-quality sensors in detail, discussing their biases, calibration challenges and the need for transparent correction procedures and comparability frameworks [4], [5]. Modern data-analytics techniques from rule-based quality control to machine-learning-based anomaly detection and time-series decomposition offer powerful tools for extracting information from such sensor streams, but they must be combined into clear and transparent workflows that operators and students can understand and reproduce. In this work we focus on a single multi-parameter air-quality node that continuously monitors temperature, humidity, particulate matter, gaseous pollutants and UV index at hourly resolution on the campus of our university. During the month of September, a Python/Flask backend receives the measurements, stores them and feeds an interactive web dashboard that runs QC rules, multivariate anomaly detection, short-term forecasting and an AI-inspired auto-calibration module. The key idea is that the system operates in two complementary modes: online, where it processes and visualizes the incoming stream in real time, and offline, where it re-analyses a full period (e.g. one month) to correct anomalies, compute indicators and evaluate performance. At the end of the month, we use the offline analysis to quantify how much the pipeline reduces the impact of rare but severe anomalies on statistics and forecasts and to prepare summarized indicators and figures that can be used for reporting, teaching and further research. In this work, we use the term auto-calibration to denote an automatic, data-driven correction step that targets clearly abnormal samples in the sensor time series (extreme spikes, heavy anomalies and small gaps). Instead of relying on an external reference instrument, the procedure exploits quality-control rules, machine-learning anomaly flags and typical hourly profiles of the sensor to replace only the problematic values with robust, median based estimates that are consistent with the usual behavior of the node.

II. Experimental Setup

The environmental node integrates sensors for temperature, relative humidity, particulate matter (PM2.5, PM10), carbon monoxide (CO), carbon dioxide (CO2), nitrogen oxides (NO, NO2) and UV index, which are connected through dedicated electronic signal-conditioning circuits. These include analogue front-end stages for amplification, filtering and level shifting, as well as protection and impedance-matching networks tailored to each sensor type, followed by analogue-to-digital conversion and a DFRobot FireBeetle 2 ESP32-E (dual-core ESP32 with integrated Wi-Fi and Bluetooth) microcontroller unit that handles local preprocessing, timing and packaging of the measurements. The microcontroller aggregates the sensor data every hour, timestamps them in local time and transmits them via a lightweight communication stack to a Python

backend through a simple API for further processing and visualization. The backend ingests the measurements, converts them to a uniform hourly time axis and stores them in a database. Figure 1 illustrates the overall experimental setup and system architecture, including the sensor node, the communication link, the Python/Flask backend and the web dashboard used for online monitoring and offline analysis.

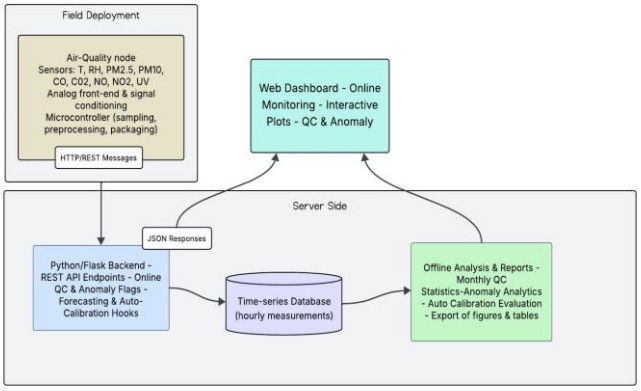

Fig. 1. Experimental setup and system architecture of the air-quality node, communication link, Python/Flask backend and web dashboard used for online monitoring and offline analysis.

For each new hour, the web dashboard updates the main time-series plot, the QC markers, the anomaly scores, the daily summary tables, the intraday profiles and the short-term forecasts. This reproduces the realistic situation where an operator or a group of students monitors a single node in real time and wants to understand what the sensors report and when they misbehave. Over the month of September, we collected 720 hourly records from the node. In the uncalibrated stream the PM2.5 values, for example, range from 6.2 to 203.6 µg/m³ with a mean of about 21.0 µg/m³, reflecting both typical background conditions and occasional extreme episodes. After applying the auto-calibration step described below, the corresponding monthly statistics for PM2.5 become much more stable, with values between 6.9 and 28.4 µg/m³, mean 17.2 µg/m³ and standard deviation 3.7 µg/m³.

III. Experimental Results

The analytics pipeline combines rule-based quality control, multivariate anomaly detection, time-series analysis and a robust auto-calibration module, all applied on the live hourly data stream from the node. Fig. 2 shows the main online time-series view and displays the raw measurements together with rule-based QC markers and ML anomaly flags for the selected sensor; this allows the operator to immediately see when values leave their typical range or when the multivariate behavior becomes unusual.

The rule-based QC layer applies simple physical limits, rate-of-change and flatline rules and consistency checks between variables. For example, UV values above 15 or temperatures above 50 °C are flagged as out-of-range, while constant readings over many hours are marked as potential sensor lockups.

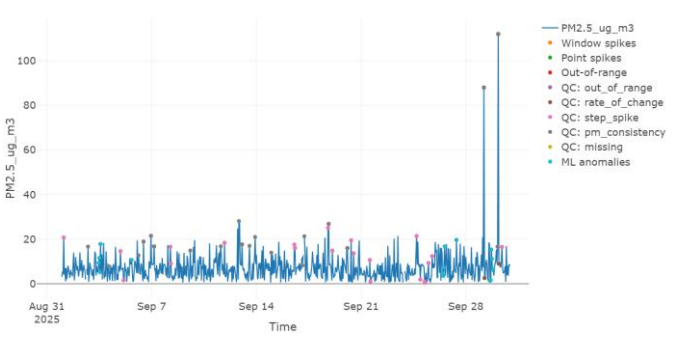

Fig. 2. Online time-series view of hourly PM2.5 over the study month, as seen by the dashboard on the live sensor data stream, with rule-based QC markers and ML anomaly flags overlaid on the raw measurements.

Daily QC statistics are summarized through a heatmap and a simple Quality Index (QI), defined as the mean number of rule violations per sample (Fig. 3). Days with large temperature and UV excursions clearly stand out with higher QC burden, even though most hours remain within normal limits.

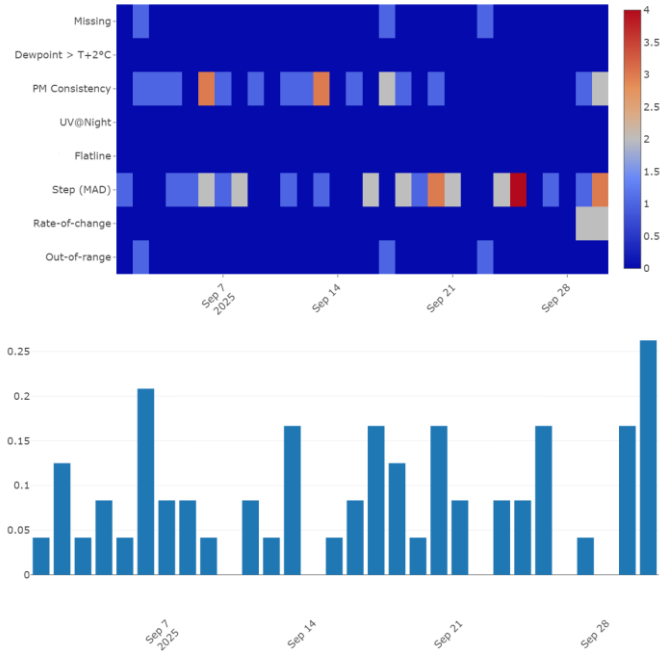

Fig. 3. Daily summary of rule-based QC results: heatmap of rule violations per day and Quality Index (QI) showing days with heavier QC burden due to large excursions in the measurements.

On top of these rules, the system computes multivariate anomaly scores using an Isolation Forest model that takes as input the current values of all sensors, time-of-day features and short rolling-window statistics. The model is trained in an unsupervised way on the same month of data and returns an anomaly score and a binary flag for each hour. This allows the dashboard to highlight not only obvious spikes but also unusual combinations of variables, such as high particulate matter without corresponding changes in gases. The evolution of

anomaly scores and the corresponding daily counts of flagged anomalies for PM2.5 are shown in Fig. 4, where clusters of anomalous behavior appear as clear bursts in the score time series and in the daily anomaly counts.

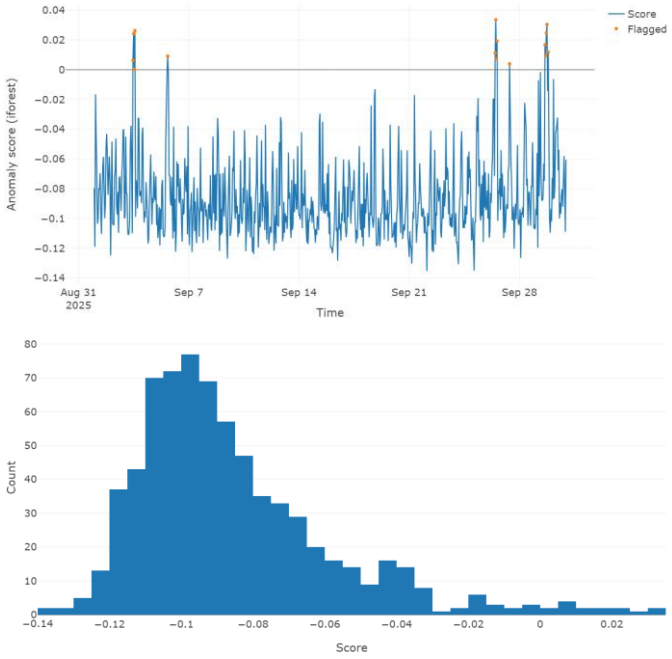

Fig. 4. Multivariate anomaly analytics for PM2.5: evolution of Isolation Forest anomaly scores and daily counts of flagged anomalies that highlight clusters of unusual behavior in the live data stream.

To better understand the relationships between variables, the system also computes a correlation heatmap over the main sensors (temperature, relative humidity, PM2.5, PM10, CO, CO2, NO, NO2 and UV index).

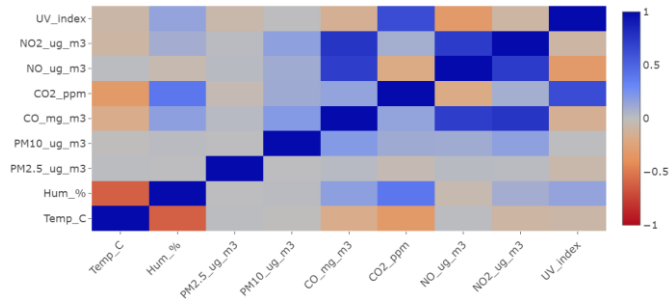

Fig. 5. Correlation heatmap between the main sensors (temperature, relative humidity, PM2.5, PM10, CO, CO2, NO, NO2 and UV index), showing the strength of pairwise linear relationships over the study period.

Figure 5 provides an at-a-glance summary of how strongly the different parameters co-vary over the study period, for example highlighting the strong association between PM2.5 and PM10 or between NO and NO2, as well as weaker or negligible correlations for variables that are driven by different processes. Such information is useful both for interpretation of events and for guiding the design of multivariate models.

For time-series analysis we apply STL decomposition and PELT-based change-point detection to the hourly PM2.5 series, separating trend, diurnal seasonality and residuals. We also fit a simple ARIMA/SARIMAX model to generate 24-hour forecasts and evaluate them in a rolling back test over the last 48 hours. In the raw stream the forecast errors are dominated by a small number of extreme PM2.5 spikes, which inflate the RMSE and distort the residuals. To address this, we apply a robust auto-calibration step on the same series. The algorithm marks as bad all samples that are out of physical range, flagged by the ML detector, missing or strong outliers relative to a seven-sample rolling median. Clean samples are used to compute a global median and a median per hour-of-day. Each bad sample is then replaced by the median of clean samples at the same hour-of-day, or by the median in a local ±6-hour window, with a fallback to the global median, and values are clipped to the physical range of the sensor. Applied to PM2.5, this procedure modifies 113 out of 720 hourly samples. In the raw stream the monthly standard deviation of PM2.5 is 23.6 µg/m³ with 55 hours above 25 µg/m³ and 18 extreme episodes above 100 µg/m³ and after auto-calibration the standard deviation drops to 3.7 µg/m³, the number of hours above 25 µg/m³ falls to 13 and there are no episodes above 100 µg/m³. Visual inspection of the corrected series confirms that the main diurnal pattern and normal day-to-day variability are preserved, while unrealistic spikes and gaps are replaced by values that are consistent with the typical behavior of the node at the same time of day as shown in Figure 6.

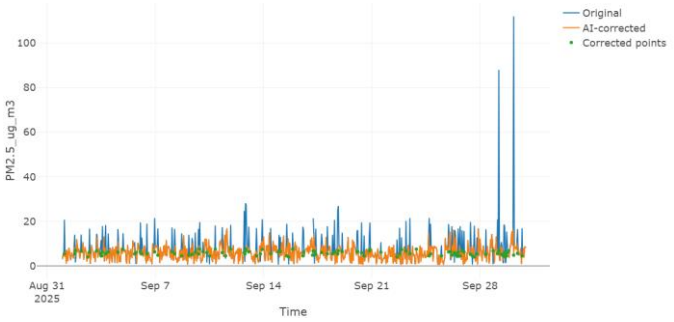

Fig. 6. Auto-calibration of the raw PM2.5 series, showing how robust median based corrections remove unrealistic spikes and gaps while preserving the underlying diurnal pattern and typical variability.

In addition to the monthly statistics, we also evaluated the effect of the auto-calibration step against a reference version of the dataset. For PM2.5, considering the 717 overlapping hourly samples, the RMSE between the raw measurements and the reference is 13.04 µg/m³, while the RMSE after auto-calibration is 12.69 µg/m³. The small change in RMSE reflects the fact that the bulk of the time series remains unaffected, whereas a very small subset of hours is heavily corrected. At the same time, the number of spike hours above the anomaly threshold used by the dashboard decreases from 6 to 0, confirming that the proposed procedure is effective at suppressing isolated extreme events

without distorting the overall diurnal pattern and background variability.

IV. Conclusion

This work demonstrates an integrated yet lightweight system for online quality control, anomaly analytics and auto-calibration of hourly air-quality data from a single IoT node. During a month-long deployment the system operates online, receiving and visualizing the live stream of measurements, flagging rule-based and multivariate anomalies and providing short-term forecasts. At the end of the period the same tools are applied offline to a complete dataset, together with a robust auto-calibration step and a quantitative evaluation of how the corrections affect statistics and episode counts. For the PM2.5 series the proposed procedure reduces the monthly standard deviation from 23.6 to 3.7 μg/m³, reduces the number of hours above 25 μg/m³ from 55 to 13 and removes all extreme episodes above 100 μg/m³ while preserving the underlying diurnal pattern. These results show that even simple median based correction strategy, combined with QC and multivariate anomaly detection, can substantially improve the trustworthiness of air-quality data without introducing a complex black-box model. The same pipeline can be used both as a practical tool for small deployments that need basic but reliable air-quality information, and as an educational platform where students can experiment with live IoT data, inject anomalies and immediately observe how data quality affects statistics, forecasts and decision making. Future work will explore more advanced forecasting models, uncertainty quantification and the extension of the auto-calibration logic to networks of nodes.

References

[1] F. Rollo, C. Bachechi and L. Po, “Anomaly Detection and Repairing for Improving Air Quality Monitoring,” *Sensors*, vol. 23, no. 2, p. 640, 2023, doi: 10.3390/s23020640.

[2] L. García, J. Lloret, P. Lorenz and J. Tomás, “Smart Air Quality Monitoring IoT-Based Infrastructure for Smart Cities,” *Sensors*, vol. 22, no. 23, p. 9221, 2022.

[3] A. A. Rahmadani, I. K. Wijaya and N. R. Hidayat, “Real-Time Air Quality Monitoring Through IoT and Web Technologies,” *Instruments*, vol. 14, no. 1, p. 2, 2024.

[4] I. Stergiou, A. Kleanthous and P. Kassomenos, “Bias Correction, Event Detection, and Temporal Pattern Discovery for Air Quality Forecast Ensembles,” *Atmosphere*, vol. 16, no. 6, p. 739, 2025.

[5] S. Shahid, M. A. Raza, M. A. Khan and A. Qamar, “Innovations in Air Quality Monitoring: Sensors, IoT and Emerging Technologies,” *Sensors*, vol. 25, no. 7, p. 2070, 2025.

Seismic Activity Detection with ESP32 Microcontroller using TinyML

George Xenofontos[1], Kyriakos Tsiakmakis[1], Argyrios T. Hatzopoulos[1], Maria S. Papadopoulou[1]*

[1] Department of Information and Electronic Engineering
International Hellenic University
57400 Sindos, Thessaloniki, GREECE
email: * mspapa@ihu.gr

Abstract*—Traditional seismic detection systems often rely on centralized processing, which introduces latency and limits deployment in remote areas. This work presents a low-cost, low-power seismic detection framework using an ESP32 microcontroller and MPU6050 sensor, leveraging TinyML for on-device inference. Key features, like zero crossing rate, cumulative absolute velocity, skewness, and dominant frequency, were extracted and fed into a lightweight Convolutional Neural Network. Testing both vibration table experiments and real-world seismic data (SCEDC) achieves 90-95% accuracy. By processing signals locally, the system minimizes latency and removes dependence on cloud infrastructure, making it suitable for remote or resource-constrained regions. Results indicate that edge-based detection via TinyML can significantly enhance earthquake early warning and structural health monitoring efforts. This system could be deployed in rural schools or bridges to provide early alerts and structural integrity assessments.

Keywords*—TinyML, Machine Learning, Embedded Systems, Microcontrollers, ESP32, CNN

I. INTRODUCTION

Recent earthquakes across various regions of the world underscore the critical need for rapid and accurate seismic monitoring. Traditional seismometer networks, while precise, often depend on centralized infrastructure, which can lead to delays in data processing and dissemination. Moreover, deploying these systems widely can be cost-prohibitive, especially in remote or resource-limited areas. Addressing these challenges requires the development of low-cost, low-power solutions that can operate independently in real time [1], [2].

Tiny Machine Learning (TinyML) on microcontrollers offers a compelling answer to these constraints. By running lightweight neural network models directly on devices such as the ESP32, which features integrated Wi-Fi, Bluetooth, and dual-core processing, real-time edge-computation becomes possible. This not only reduces reliance on cloud connectivity but also ensures minimal latency in detecting seismic events [3]. Our work leverages the built-in MEMS sensor MPU6050 to capture vibrations and utilizes a specially designed convolutional neural network (CNN) optimized for the microcontroller's limited resources.

The main objective of this study is to investigate whether a TinyML-based seismic detection framework can accurately distinguish between everyday structural vibrations and genuine earthquake activity. By developing a compact CNN model, we demonstrate that it is feasible to carry out effective signal filtering, feature extraction, and classification on a constrained platform, all while maintaining high accuracy. This integrated system contributes to the field of earthquake early warning by offering an accessible, scalable alternative to conventional seismology networks. Ultimately, our approach shows promise for improved disaster preparedness and resilience, particularly in underserved or remote communities at risk of seismic hazards.

II. RELATED WORK

Recent advances in the Internet of Things (IoT) and embedded systems have enabled the development of smart seismic monitoring solutions. MEMS-based sensors, such as accelerometers and gyroscopes, have become popular due to their affordability, compact size, and sensitivity to ground motion [3]. Projects like CrowdQuake [4] and LightEQ [5] have demonstrated the feasibility of using distributed sensor networks for earthquake detection, leveraging edge computing to reduce latency and improve scalability.

Machine learning has also played a transformative role in seismic signal analysis. Traditional algorithms like STA/LTA have been widely used for event detection but often struggle with noisy environments and require manual tuning [6]. In contrast, deep learning models, particularly Convolutional Neural Networks (CNNs), have shown superior performance in distinguishing seismic events from background noise. Meier et al. [7] achieved over 99% accuracy using CNNs trained on the SCEDC dataset, highlighting the potential of data-driven approaches in earthquake early warning systems.

Tiny Machine Learning (TinyML) extends these capabilities to resource-constrained devices by enabling on-device inference. This paradigm shift allows models to run directly on microcontrollers, eliminating the need for continuous cloud connectivity. Recent works have explored TinyML for environmental sensing, structural health monitoring, and vibration analysis [8], [9]. However, few studies have applied TinyML specifically to seismic detection.

Our work builds upon these foundations by integrating a MEMS sensor (MPU6050) with an ESP32 microcontroller and deploying a compact CNN model using TensorFlow Lite. Unlike prior approaches that rely on cloud-based processing or high-end hardware, our system performs real-time classification locally, offering a scalable and cost-effective solution for earthquake monitoring in underserved regions.

III. METHODOLOGY

This section describes the overall design and implementation framework for our seismic detection system, including the hardware architecture, data processing strategies, feature engineering, and the machine learning model optimized for TinyML deployment.

A. Hardware Setup

We employ an ESP32 microcontroller. It was selected for its dual-core processing up to 240 MHz, integrated Wi-Fi and Bluetooth, and low power consumption. It offers sufficient computational capacity to run lightweight neural networks on the edge without continuous cloud support [10]. For vibration sensing, we use the MPU6050, a 6-axis MEMS device integrating a 3-axis accelerometer and 3-axis gyroscope. Its high sensitivity to small accelerations makes it suitable for capturing detailed seismic waveforms [11].

B. Software Overview

Data from the MPU6050 is read in real time via the I2C interface and fed into a TinyML pipeline on the ESP32. We utilize TensorFlow Lite Micro for on-device inference. Sensor signals first undergo noise filtering and feature extraction before being classified by a compact convolutional neural network (CNN). By processing data locally, the system minimizes latency and functions independently of external servers, which is crucial in areas lacking reliable internet connections.

C. Data Collection and Preprocessing

For controlled testing, we place the MPU6050 on a vibration table to simulate a range of oscillation patterns, from low-intensity noise to more pronounced seismic-like shaking. These controlled experiments enable us to calibrate the sensor and validate system responsiveness. We also incorporate real-world seismic data from the Southern California Earthquake Data Center (SCEDC) to assess the model's performance in realistic scenarios [12].

To reduce signal artifacts, we apply high-pass and low-pass filters. The high-pass filter eliminates very low-frequency drift, while the low-pass filter smooths out transient spikes. This combined approach isolates the frequency range most indicative of earthquakes. Normalization techniques like min-max scaling further ensure consistent data inputs to our model.

D. Feature Extraction

We compute domain-specific features known to be effective in characterizing ground motion. These include:

- **Zero Crossing Rate (ZCR):** Reflects how frequently the signal crosses the zero-amplitude line, useful for discerning different vibration types.
- **Cumulative Absolute Velocity (CAV):** Aggregates signal intensity over time, capturing the overall energy of a seismic event.
- **Skewness:** Measures the asymmetry of the signal distribution, which can distinguish certain waveforms from noise.
- **Predominant Frequency (TauC):** Highlights the signal's dominant frequency component, helping differentiate quake-induced vibrations from typical building movements.

These features significantly reduce raw data complexity, providing a compact, informative input for the classifier.

E. CNN Model and Training

Our CNN is designed with minimal layers, convolution, pooling, and a fully connected layer, suitable for the ESP32's resource constraints which is shown in Fig. 1. ReLU activations introduce non-linearity, while max-pooling downsamples feature maps to avoid overfitting. We train the network on a workstation using batches of data (batch size of 32) for 10-20 epochs. An Adam optimizer with binary cross-entropy as the loss function balances efficient convergence with reliable classification.

After achieving satisfactory performance, we quantize the model and convert it to a TensorFlow Lite Micro format. Specifically, we employed 8-bit integer quantization for the model's weights and activations, reducing memory footprint to fit within the ESP32's on-chip resources. This process preserves most classification accuracy while significantly lowering storage and runtime demands. Once flashed onto the microcontroller, the final model infers in real time, labeling incoming vibrations as either normal noise or potential seismic events.

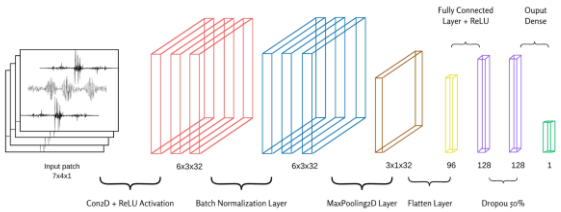

Fig. 1. CNN model architecture in visual representation

IV. RESULTS AND DISCUSSION

This section highlights both the controlled and real-world performance of our seismic detection system, emphasizing the model's robustness and potential limitations.

A. Controlled Experiment Findings

To validate the core functionality, we initially tested the system on a vibration table, simulating a range of low- to high-frequency oscillations. The results showed that the ESP32-MPU6050 setup accurately distinguished mild vibrations (e.g., building sway or ambient noise) from higher-intensity waveforms designed to mimic seismic events.

Detection Accuracy: On synthetic "quake" vibrations, the classifier achieved an average accuracy of 93% across multiple trials, indicating strong signal differentiation. For purely noise-induced samples, misclassifications occurred primarily in borderline amplitudes where sensor readings were near the detection threshold.

B. Real-World Data Analysis

Next, we assessed performance using seismic data from the Southern California Earthquake Data Center (SCEDC). We extracted key featuresm ZCR, CAV, Skewness, and TauC, from event waveforms, then tested them against the trained CNN model running under TinyML constraints.

Performance metrics:

- Accuracy: 90-95% range, depending on the quake magnitude and noise levels
- Precision: 91%, indicating strong reliability in identifying true quakes
- Recall: 90%, most seismic events were correctly caught by the system
- F1-score: ~90.5%, a balanced measure combining precision and recall
- ROC-AUC: 0.99, very high discriminative power across different thresholds

Our approach aligns closely with reported precision/recall values in prior machine learning-based seismic detection studies. Systems leveraging more extensive computational resources sometimes show slightly higher accuracy (exceeding 95%), but they typically require cloud processing and are less suitable for low-power deployments.

C. *Observations*

- The system achieves near state-of-the-art performance, while running on a low-power microcontroller.
- Local inference reduces latency and dependence on external servers, critical in areas with unreliable network coverage.
- Occasional false positives in borderline cases, where environmental oscillations overlap with quake-like frequency ranges.
- Quantization, while necessary for TinyML, introduces slight reductions in precision, especially on small amplitude signals.

V. Conclusion and Future Work

In summary, this research has demonstrated the feasibility of TinyML-based seismic detection using an ESP32 microcontroller and MPU6050 sensor. Our findings show that a compact convolutional neural network can accurately classify seismic events in real time, even under strict resource constraints. With detection accuracy around 90-95%, as shown in Fig. 2, the system offers a promising foundation for low-cost, edge-based earthquake monitoring solutions.

From an application standpoint, the ability to run inference locally has significant implications for earthquake early warning systems, especially in settings where network infrastructure is limited or unreliable. As a low-power, stand-alone detector, the proposed platform could be integrated into a broader IoT ecosystem or used for structural health monitoring, offering insights into a building's stability under stress.

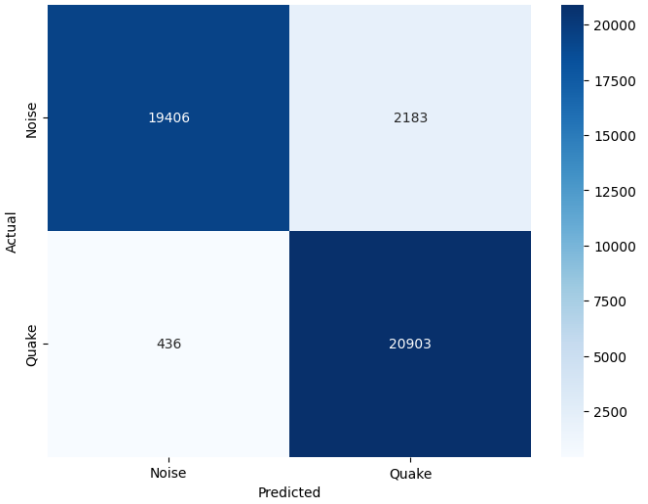

Fig. 2. Confusion Matrix metrics

Despite encouraging results, several enhancements would strengthen this approach. First, sensor calibration can be refined to reduce noise-induced false positives, particularly in borderline amplitude ranges. Second, the system's scalability can be explored by deploying larger sensor networks, potentially increasing overall coverage and detection granularity. Furthermore, adopting more advanced ML architectures such as recurrent neural networks (RNNs) or Transformers, tailored for time-series data, could lead to higher accuracy, though memory constraints would need careful management. Finally, testing in varied seismic zones around the globe would validate the model's robustness and reveal further opportunities for localized calibration and improved feature extraction.

References

[1] R. Duggal et al., "Building structural analysis based Internet of Things network assisted earthquake detection," Internet of Things, vol. 19, p. 100561, Aug. 2022, doi: 10.1016/j.iot.2022.100561.

[2] S. Elizabeth Philip and M. Helen Santhi, "Peak Ground Acceleration Analysis using Past Earthquake Data," J. Phys.: Conf. Ser., vol. 1716, no. 1, p. 012013, Dec. 2020, doi: 10.1088/1742-6596/1716/1/012013.

[3] I. Khan, S. Choi, and Y.-W. Kwon, "Earthquake Detection in a Static and Dynamic Environment Using Supervised Machine Learning and a Novel Feature Extraction Method," Sensors, vol. 20, no. 3, p. 800, Feb. 2020, doi: 10.3390/s20030800.

[4] M. Abdalzaher, M. Krichen, D. Yiltas-Kaplan, I. Ben Dhaou, and W. Adoni, "Early Detection of Earthquakes Using IoT and Cloud Infrastructure: A Survey," Sustainability, vol. 15, no. 15, p. 11713, July 2023, doi: 10.3390/su151511713.

[5] T. Zainab, J. Karstens, and O. Landsiedel, "LightEQ: On-Device Earthquake Detection with Embedded Machine Learning," in Proceedings of the 8th ACM/IEEE Conference on Internet of Things Design and Implementation, San Antonio TX USA: ACM, May 2023, pp. 130–143. doi: 10.1145/3576842.3582387.

[6] Y.-M. Wu et al., "A High-Density Seismic Network for Earthquake Early Warning in Taiwan Based on Low Cost Sensors," Seismological Research Letters, vol. 84, no. 6, pp. 1048–1054, Nov. 2013, doi: 10.1785/0220130085.

[7] M. Meier et al., "Reliable Real-Time Seismic Signal/Noise Discrimination With Machine Learning," JGR Solid Earth, vol. 124, no. 1, pp. 788–800, Jan. 2019, doi: 10.1029/2018JB016661.

[8] O. M. Saad et al., "SCALODEEP: A Highly Generalized Deep Learning Framework for Real-Time Earthquake Detection," JGR Solid Earth, vol. 126, no. 4, p. e2020JB021473, Apr. 2021, doi: 10.1029/2020JB021473.

[9] S. Prakash et al., "Is TinyML Sustainable?," Commun. ACM, vol. 66, no. 11, pp. 68–77, Nov. 2023, doi: 10.1145/3608473.

[10] A. Pradeep, A. Latifov, A. Yodgorov, and N. Mahkamjonkhojizoda, "Hazard Detection using custom ESP32 Microcontroller and LoRa," in 2023 International Conference on Computational Intelligence and Knowledge Economy (ICCIKE), Dubai, United Arab Emirates: IEEE, Mar. 2023, pp. 36–40. doi: 10.1109/ICCIKE58312.2023.10131784.

[11] Neneng Triyunita, Catur Edi Widodo, and Jatmiko Endro Suseno, "Development of Vibration Detection Prototype Using MPU6050 For Building Durability Evaluation," IJSRST, pp. 126–134, Nov. 2023, doi: 10.32628/IJSRST52310620.

[12] SCEDC, "Southern California Earthquake Data Center." Caltech, 2013. doi: 10.7909/C3WD3XH1.

Parameterizable FPGA Accelerator Design for Embedded Deep Learning (INVITED)

Panagiotis Mousouliotis
School of Informatics
Aristotle University of Thessaloniki
e-mail: pmousouliotis@csd.auth.gr

Abstract: Field-Programmable Gate Arrays (FPGAs) provide a compelling platform for energy-efficient deep learning at the edge, yet their flexibility often comes at the cost of high design complexity. This talk presents a hardware–software co-design methodology for creating parameterizable convolutional neural network (CNN) accelerators using high-level synthesis (HLS) tools (Fig. 1). The proposed approach [1] enables designers to systematically tune architectural parameters, such as channel parallelism, memory partitioning, and operating frequency, according to application-level constraints on latency, power, and resource usage.

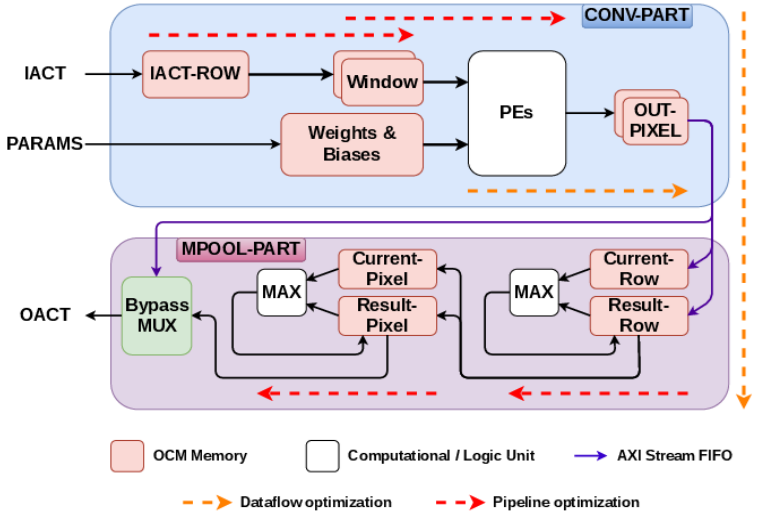

Fig. 1. CNN accelerator

Acknowledgment: This work is part of R-PODID project, supported by the Chips Joint Undertaking and its members, including the top-up funding by National Authorities of Italy, Turkey, Portugal, The Netherlands, Czech Republic, Latvia, Greece, and Romania under grant agreement No 101112338.

[1] Mousouliotis, Panagiotis, and Georgios Keramidas. "A Parameterizable Convolution Accelerator for Embedded Deep Learning Applications." In 2025 IEEE Computer Society Annual Symposium on VLSI (ISVLSI), vol. 1, pp. 1-6. IEEE, 2025.

Bio: Panagiotis Mousouliotis holds a Ph.D. in Embedded Systems and has over a decade of hands-on experience in designing and deploying AI accelerators and embedded systems. His professional journey spans roles in both industry and academia, where he has worked on reconfigurable computing platforms and FPGA-optimized deep-learning solutions. With a strong foundation in electrical and computer engineering, his work bridges algorithmic development, hardware design, and real-time deployment in resource-constrained environments.

Erasmus+ MSc Course: Intelligent Sustainable Habitats masters course

Filliana Anagnostaki, Theodoros Kosmanis [0000−0002−8730−1345] and Dimitrios Tziourtzioumis [0000−0002−1881−3953]
Laboratory of Energy Systems, Department of Industrial Engineering and Management, International Hellenic University, Alexander University Campus, 57400 Sindos, Greece
filliana.anagnostaki@gmail.com

Abstract

The "Intelligent Sustainable Habitats masters course" (INHABITAT) project aims to develop an advanced interactive certified 2-year MSc course related to IoT applications in everyday life that will train individuals with the necessary skills & knowledge to work in the rising “Intelligent Sustainable Habitats” industry. The course is also formulated to stimulate transversal competences such as the increased sense of initiative & entrepreneurship. The course is designed to follow the European Credit Transfer & Accumulation System (ECTS) credit standards for certification recognition across the European Union (EU).

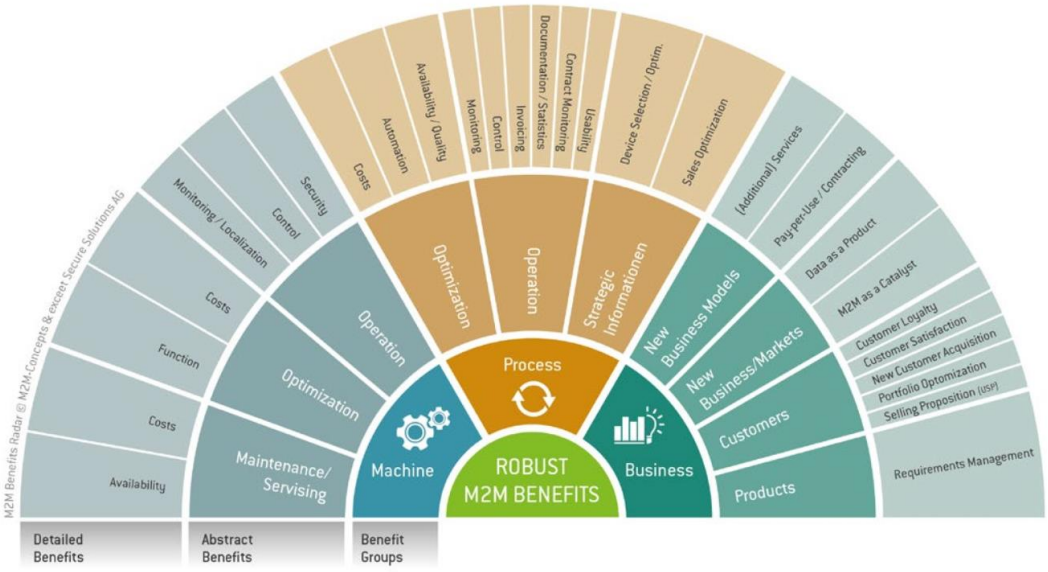

Figure 1. Machine to Machine (M2M) direct intercommunication services.

The developed syllabus will also be offered via vocational education and training in the form of micro-credentials to those who wish to gain specific skills for up-skilling and life-long education.

The innovative curriculum comprises interactive teaching methods and partnerships with expert academic and Internet of Things (IoT) expert organizations in order to give to 40 students a solid background for starting a fruitful career in the industry.

Besides the main and ultimate objective of INHABITAT project, i.e. the development and piloting implementation of a postgraduate study program on urban sustainable development, other smaller objectives need to be obtained, like:

- the synchronization and cooperation of a numerous number of teachers from all around Europe,
- the accreditation of the MSc program requiring significant efforts and time as the postgraduate study program accreditation was made in full accordance with the Lithuanian legislation,
- the development of an e-learning platform for asynchronous communication of the teaching personnel with the students.

All the objectives, efforts and outcomes in the frame of an Erasmus project procedures are analyzed in this work.

References

[1] European Commission: Renewable energy directive (ec.europa.eu/energy/en/topics/renewable-energy/renewable-energydirective/overview).

[2] Grand View Research: Environmental Monitoring Market Size (grandviewresearch.com/industry-analysis/environmentalmonitoring-market).

[3] Proposal number 101108631, “Intelligent Sustainable Habitats masters course (INHABITAT)”, ERASMUS-EDU-2022-PI-ALL-INNO.

HORIZON-MSCA project: Integration of Advanced Experiments, Computation and Data for Innovation in Freeze Casting and Advanced Porous Structures

Theodoros Kosmanis [0000−0002−8730−1345] and Dimitrios Tziourtzioumis [0000−0002−1881−3953]
Laboratory of Energy Systems, Department of Industrial Engineering and Management, International Hellenic University, Alexander University Campus, 57400 Sindos, Greece
kosmanis@ihu.gr

Abstract

ICE-Link project aims to collaboratively research on ice-templating of advanced porous materials through modern data system sharing, experiments and numerical/physical modelling. The project establishes systematic data of ice-templated porous materials and predictive modelling supported by machining learning for establishing detailed structures-properties relationship. The project investigates the cooling process through experimental, phased field modelling and molecular simulation for ice/emulsion structure growth/evolution process. The data and advanced modelling approach established are used to develop porous systems with tunable porosities for advanced applications. One key area is to control porosity and distribution to achieve uniform porosities or gradient/hierarchical structures in functional ceramics (carbon, pizeoceramics, BCZY (Barium Cerium Zirconium Yttrium oxide) - GDC (Gadolinium-Doped Ceria) ceramics for fuel cells, membrane for hydrogen separation, etc.). Another area is to develop tunable pore size/shape and porosity in monoliths, beads, and fibres of plastics (e.g. for PLA (PolyLactic Acid) scaffolding, etc.).

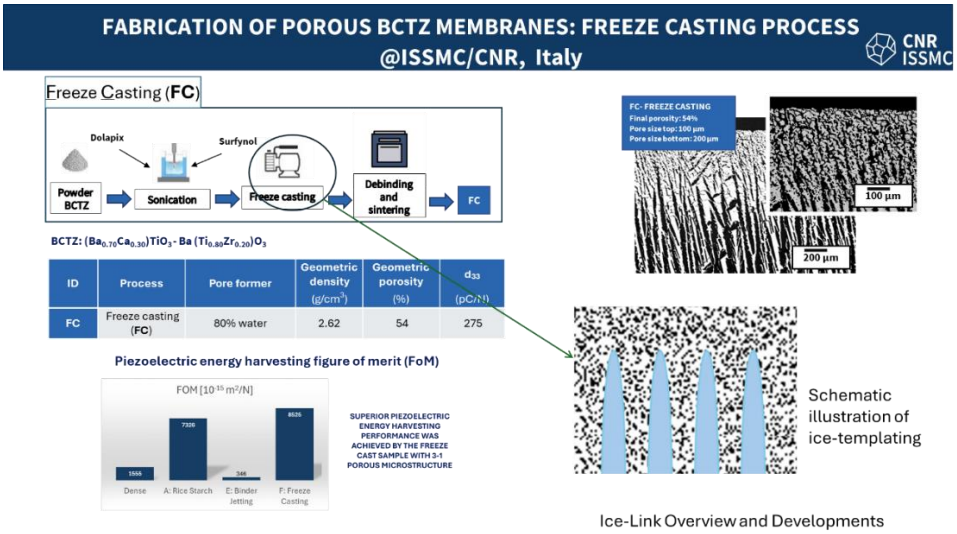

Figure 1. Fabrication process of porous BCTZ (Barium Cerium Titanate Zirconate) membranes.

The resulted advanced data system, intelligent modelling program, new materials and improved scientific understanding are meant to contribute to the research and innovation capacity in Europe and the world on ice-templating, porous materials and associated systems with a long term economic and social impact. The international network of academic and industrial partners is expected to serve as a pivoting platform for future data sharing, research and innovation, speeding up material or product development cycle through interdisciplinary research. It will enhance the Research and Innovation (R&I) capacity of academic and industrial partners, sustain the effort in collectively challenging issues in this most active research area and jointly developing major break-through technologies. Details on the procedures and the results of the ICE-Link Marie Curie, European project are provided in this work, presenting the technological achievements and aspects behind it.

References

[1] H. Zhang, “Ice Templating and Freeze-Drying for Porous Materials and Their Applications”, Wiley- VCH Verlag GmbH & Co, 2018.

[2] S. Mouradian, “Simulating Ice Processes using the finite element unstructured adaptive model fluidity”, PhD Thesis, UCL (London), 2015.

[3] Proposal number 101130406, “Integration of Advanced Experiments, Computation and Data for Innovation in Freeze Casting and Advanced Porous Structures (ice-Link)”, HORIZON-TMA-MSCA-SE, 2022.

Erasmus+ MSc Course on smart sustainability solutions

Dimitrios Tziourtzioumis [0000−0002−1881−3953] and Theodoros Kosmanis [0000−0002−8730−1345]
Laboratory of Energy Systems, Department of Industrial Engineering and Management, International Hellenic University, Alexander University Campus, 57400 Sindos, Greece
dtziour@ihu.gr

Abstract

A set of “smart” devices are infiltrating every level of our lives, forming the Internet of Things (IoT), a network of physical devices embedded with electronics, software, sensors and actuators allowing interconnectivity and exchange data without human intervention. Sustainability IoT transformation is storming the socio-ecological domain ranging from applications in environmental monitoring, waste handling, resource management and protection, green cities to renewable energy production. People with no educational background specific related to Sustainability IoT systems are currently designing, developing, installing, servicing and maintaining the systems that have and will enter the market. There is a Global shortage of trained engineers and technicians to cater and handle this new technology, especially in the European Union (EU).

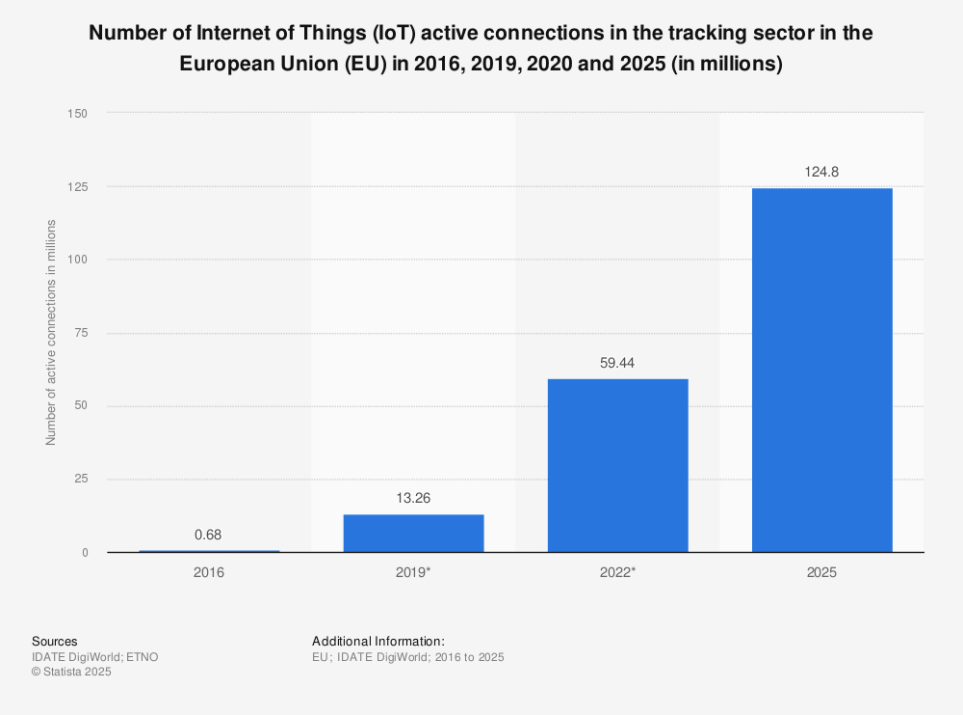

Figure 1. IoT active connections in the EU 2016, 2019, 2020 and 2025.

The mastErs COurse on smart sustainability soLUTIONs (ECOLUTION) will develop an advanced interactive MSc course related to Sustainability IoT Engineering to train individuals with the skills and knowledge to work in the rising “Smart Sustainability” industry. The course will foster transversal competences like initiative and entrepreneurship. It complies with the European Credit Transfer and Accumulation System (ECTS). In this work, all the efforts for the achievement of the objectives and the outcomes of the first reporting period are analysed. Important conclusions on the actual implementation are made, revealing difficulties and good practices of European educational programmes.

References

[1] Z. Saadati, R.V. Barenji, “Toward Industry 5.0: Cognitive Cyber-Physical System”, Springer Nature Singapore, 2023.

[2] A. Raza et al., “Impact of Climate Change on Crops Adaptation and Strategies to Tackle Its Outcome: A Review”, Plants, vol. 8,2 34. 30 Jan. 2019, doi:10.3390/plants8020034

[3] Proposal number 101140050, “mastErs COurse on smart sustainability soLUTIONs (ECOLUTION)”, ERASMUS-EDU-2023-PI-ALL-INNO.